This is a repository copy of *Influence of pore fluid on grain-scale interactions and mobility of granular flows of differing volume*.

White Rose Research Online URL for this paper:
https://eprints.whiterose.ac.uk/193920/

Version: Published Version

JGR Earth Surface

AGU
ADVANCING EARTH AND SPACE SCIENCE

Key Points:
- Dry granular flows of five volumes between 0.2 and 1.0 m^3 observed to yield a constant effective friction in flume tests
- Saturated flows of the same granular material exhibited a nonlinear decrease in effective friction with increasing volume
- Results provide unique test scenario for simulations by constraining friction properties prior to exploring pore fluid effects

Supporting Information:
Supporting Information may be found in the online version of this article.

Correspondence to:
W. A. Take,
Andy.Take@queensu.ca

Influence of Pore Fluid on Grain-Scale Interactions and Mobility of Granular Flows of Differing Volume

Alexander M. Taylor-Noonan[1], Elisabeth T. Bowman[2], Brian W. McArdell[3], Roland Kaitna[4], Jim N. McElwaine[5], and W. Andy Take[1]

[1]Department of Civil Engineering, Queen's University at Kingston, Kingston, ON, Canada, [2]Department of Civil Engineering, University of Sheffield, Sheffield, UK, [3]Swiss Federal Institute for Forest, Snow and Landscape Research (WSL), Zürich, Switzerland, [4]Institute of Mountain Risk Engineering (IAN-BOKU), University of Natural Resources and Life Sciences, Vienna, Austria, [5]Department of Earth Sciences, Durham University, Durham, UK

Abstract The presence of a pore fluid is recognized to significantly increase the mobility of saturated over dry granular flows. However, the mechanisms through which pore fluid increases mobility may not be captured in experimental flows of small volume typical of laboratory conditions. Here we present the results of dry and initially fluid saturated or "wet" experimental flows of near-monodisperse coarse-grained ceramic particles in a large laboratory flume for five source volumes of 0.2–1.0 m^3. Measurements include flow height, velocity profile, pore pressure, and evolving solid volume fraction, as well as the final deposit shape. The dry experiments constrain the frictional properties of the common granular material and comparison with wet flows permits an independent evaluation of the interstitial fluid effects. These results demonstrate that flow dilation and strong variation in the velocity profile are directly linked to a greatly increased mobility for wet granular flows compared to dry, and a significant influence of scale as controlled by source volume on flow behavior. Excess pore pressure need not be present for these effects to occur.

Plain Language Summary An accurate prediction of how fast and how far a landslide, such as a debris flow, will travel is essential to define the hazard posed to life and property by these geophysical flows. While dry frictional flows often behave according to the simple physics of friction resisting motion, initially water saturated granular flows tend to travel farther and faster than the same scenario under dry conditions. In this paper, we explore this phenomenon in detail, using comparatively large-sized monodisperse grains, in which we expect the pore fluid effects to be limited to buoyancy. We undertake high-speed video analysis to examine differences in grain-scale behavior that might lead to increased mobility in saturated over dry flows, and scan the deposit shape to quantify how far the debris travels. Large flume tests comparing dry versus saturated flows for five source volumes of 0.2–1.0 cubic meters reveal that, in contrast to dry flows, saturated flows travel significantly farther as the volume of the landslide increases. This occurs even while the pore fluid pressure acts only to provide buoyancy in the flow. This data is unique as it will enable researchers to test how well numerical simulations are able to model the travel behavior of the same material in a dry and water saturated state.

1. Introduction

The quantification of the hazard posed by a potential landslide source volume requires an accurate prediction of the travel path and distal reach of the final deposit. This is generally accomplished in practice by using runout observations from past landslide events in the same location or similar geologic materials to delineate potential hazard areas for future landslides. These observations are then used either within an empirical-statistical approach to define runout exceedance probability (Legros, 2002) or by inferring material rheological models and parameters from numerical simulations to match runout and inundation depth trimlines of historical events (McDougall, 2017). Heim's Ratio (*H/L*) was an early empirical-statistical proposal of a parameter for risk assessment by geometrical similarity (Figure 1). The total runout length *L* can be decomposed into contributions from the translation of the center of mass L_{COM} and spreading of the material ahead of the center-of-mass S_f (Dade & Huppert, 1998; Staron & Lajeunesse, 2009), as well as the distance from the back of the head scarp to the source center of mass. The difference in elevation, *H*, is measured from the back of the head scarp to the front of the deposit. The total runout length *L* is typically of greatest interest for hazard assessment whereas the potential energy of the source volume is often equated to *H*. The travel angle $\alpha_g = \arctan(H_{COM}/L_{COM})$ is defined as the

Writing – original draft: Alexander M. Taylor-Noonan
Writing – review & editing: Alexander M. Taylor-Noonan, Elisabeth T. Bowman, Brian W. McArdell, Roland Kaitna, Jim N. McElwaine, W. Andy Take

angle of inclination between the center of mass of the runout deposit and the center of mass of the source volume and has been associated with an apparent friction coefficient (e.g., Parez & Aharonov, 2015). Conceptually, the travel angle may be invariant with source volume (Figure 1b), or it may vary with the source volume (Figure 1c) where scale effects are significant.

Debris flows are very rapid to extremely rapid flow events of material that is of low plasticity, unsorted and mixed (Hungr et al., 2013). The flows often contain interstitial fluid (water, sometimes with suspended clay and silt particles) and even coarse material can exhibit liquefied behavior. Aggregated observations of historical debris flows, compiled by Corominas (1996) and Rickenmann (2011), illustrate the general trend of decreasing travel angle (signifying increased mobility and a decrease in effective flow resistance) as source volume increases. While there is a lack of consensus in the literature, collisionality (e.g., Armanini, 2013), fragmentation (e.g., Bowman et al., 2012; Caballero et al., 2014), pore pressure diffusion length-scales (e.g., Iverson, 2015; Kaitna et al., 2016), and thermal effects (e.g., Alonso et al., 2016; Fischer et al., 2018; Goren & Aharonov, 2007; Voight & Faust, 1982) amongst other hypotheses (e.g., effects at the laboratory scale such as side wall effects and air drag; Bryant et al., 2015; Kesseler et al., 2020) have been investigated as potential mechanisms through which larger volume landslides achieve higher mobility. Here, we wish to explore the behavior of the coarse particles both in a dry state and with interstitial water, over a range of source volumes, to observe the effect on travel velocity and runout length.

Experimental flume flows using dry granular material have shown that when the rheology of the flow is very simple, the runout behavior can be straightforwardly related to general physical parameters like slope angle, basal friction and grain size (e.g., Mangeney et al., 2010) or predicted using depth-averaged models (e.g., Bryant et al., 2015). Flows of fully saturated or initially saturated materials have shown changes in flow resistance with source volume (e.g., de Haas et al., 2015), fines content or moisture content (e.g., Hürlimann et al., 2015; Kaitna et al., 2014; Zhou et al., 2018).

Numerical simulations of landslide runout offer the ability to release a source volume, propagate its flow over a 2D or 3D geometrical representation of the terrain, and provide estimates of inundation depth, velocity, and definition of the maximum distal reach of the deposit for a given pairing of a resistance law and respective model parameter(s). In the case, the moving mass is modeled based on an equivalent fluid concept (Hungr, 1995), the resistance law is chosen based on the nature of the flow. That can range from a granular flow to a fully liquefied flow for which the effect of pore fluid is of major importance.

For granular flows, the main source of flow resistance stems from particle friction and particle collisions. In dense granular flows, particle contacts are long-lasting and force chains develop. For natural flows in a frictional regime, the recently developed $\mu(I)$ rheology may be appropriate (Forterre & Pouliquen, 2008). A collisional regime can occur when the concentration of solids, represented by the volume fraction ν as the portion of total volume occupied by solid particles, is too low to maintain these long-lasting contacts (Bagnold, 1954; Jenkins & Savage, 1983). In a collisional regime the flow resistance is dependent on ν and the rate of collisions (e.g., Lun & Savage, 1986). The transition between these idealized regimes is not abrupt and the regimes are thought to exist simultaneously in the transition (Ancey & Evesque, 2000; Armanini, 2013). The interstitial fluid would also affect this collisional-frictional network of discrete particles.

With the addition of an interstitial fluid to a granular flow, particles are subject to both buoyancy and drag forces (Armanini, 2013; Iverson, 1997). Particle buoyancy reduces the interparticle stresses, which is represented on a macro scale by the concept of geotechnical effective stress $\sigma' = \sigma - u$, where σ is total stress, u is pore pressure. In a frictional continuum material, the shear resistance from friction is proportional to the effective stress (e.g., $\tau = \sigma' \tan \phi'$) - that is, the Mohr-Coulomb criterion.

For a fully liquefied or low solids content flow, the effect of interstitial fluid may be more conveniently modeled by a non-Newtonian phenomenological flow law (Ancey, 2007), which is characterized by a distinct velocity profile. In both cases, pore pressure effects are typically considered to be non-transient during the duration of the flow. The validity of this assumption has been explored in Tayyebi et al. (2021), who suggest model choice should be guided through a consideration of two competing characteristic times: (a) consolidation time and (b) propagation time. For scenarios in which the time of pore pressure dissipation is rapid in comparison to the travel time, the high permeability material is unlikely to retain excess positive pore pressure (e.g., Iverson, 2015; Kaitna et al., 2016; Pastor et al., 2014; Pudasaini et al., 2005), permitting simpler models of pore pressure effects to be
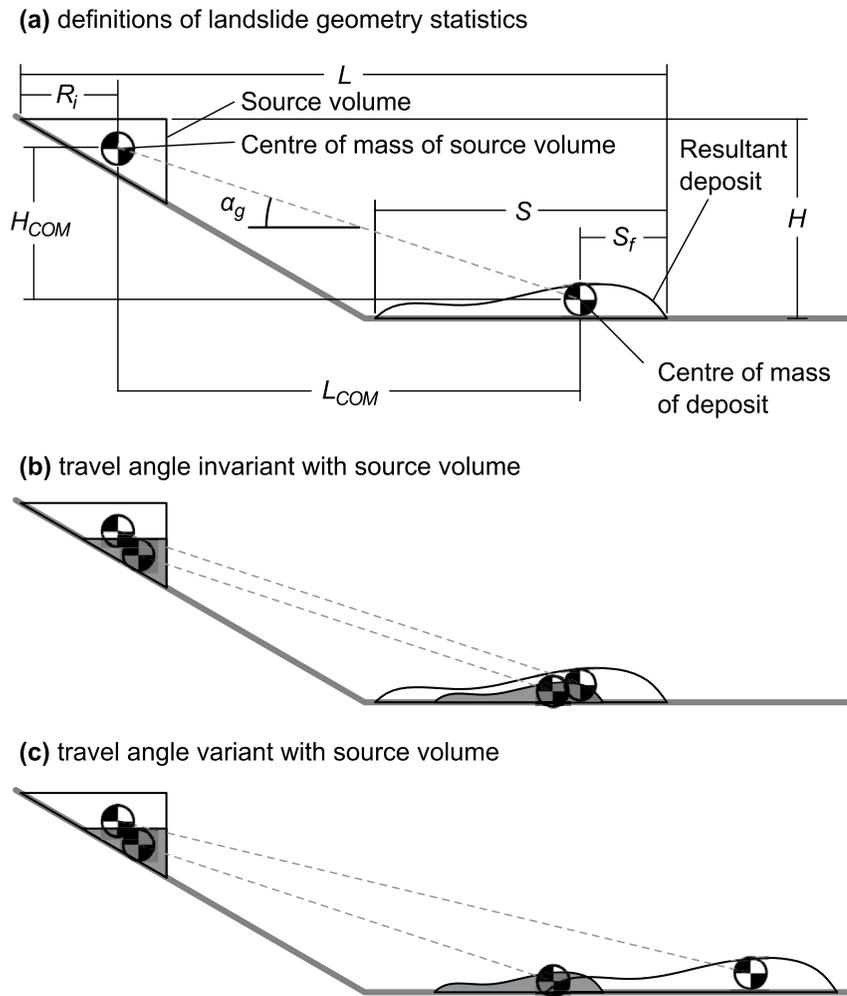
Figure 1. Schematic illustration of flows in a simple planar flume, showing (a) definition of geometry statistics, (b) the case where the travel angle α_g is invariant with source volume, and (c) potential variation of α_g with changing source volume indicating a variation of flow resistance.

used. On the other hand, it may be appropriate for fully undrained models to simulate lower permeability flows, such as high water content slurries or liquefied debris. Debris flows with intermediate permeability between these two end members have the most computationally complex requirements for numerical simulation as the consolidation time and travel time can be of the same order, and pore pressure can vary with space and time.

Recent observations of large landslide events which include a transition from a granular flow to a liquefied flow (e.g., Shugar et al., 2021; Walter et al., 2020) and progress in monitoring of debris flows, including basal stresses (e.g., McArdell et al., 2007) and velocity profiles (Nagl et al., 2020) highlight the importance of the fluid in granular flows.

The addition of an interstitial fluid is therefore recognized to have a dominant impact on the mobility of the flow. Impulse releases of an opaque material from behind a rapidly opening gate have been performed by the USGS (e.g., Iverson et al., 2010) on a large scale with a laterally unconfined runout area or at laboratory scale (e.g., Baselt et al., 2022; Hürlimann et al., 2015). Flows may also be triggered by moving water (e.g., Hotta, 2012; Lanzoni et al., 2017; Lyu et al., 2017; Tsubaki et al., 1983; Zheng et al., 2021). A recirculating flume was used by Armanini et al. (2005) to host a long-duration debris flow from which grain-scale measurements of volume fraction and velocity could be taken.

However, experimental studies in which both the bulk-scale (runout) and grain-scale behavior of identical granular material in a dry and saturated initial state are directly compared are rare. The comparison would provide

a unique opportunity to test numerical simulation outcomes by first constraining the frictional properties of the material (i.e., matching the runout behavior of the dry experiments of different source volumes) before independently evaluating the implementation of rheological models to account for buoyancy, fluid drag, and pore pressure affecting the frictional material. The relative contributions of each mechanism may be revealed after systematically matching the experimental results at each source volume.

We performed a series of experiments on the end member cases of high permeability granular material which is initially dry or initially saturated with the objective of defining the influence of interstitial fluid and landslide volume on the runout distance and the relative contributions of translation and spreading in a material in which excess pore pressure is not expected to occur. A monodisperse material was used to ensure no segregation of particle size would take place during flow which could alter the rheologic behavior, other than that caused by variation in solid and fluid concentration. Granular material was selected of a large enough grain size such that excess pore pressures did not occur and that the effects of the interstitial fluid would theoretically be limited to buoyancy and drag. A large grain size is also suitable for identifying particles on high-speed video, from which observations of contact behavior and flow regimes can be made. Each flow was initiated from a well-defined state and observed comprehensively during the travel and arrest phases. Dry flows of the identical source volumes were also tested as a direct point of reference for comparison.

In the remainder of the manuscript, we first describe the research flume, instrumentation, and high-speed video analysis methods used for the experiments. The flow regimes of both dry and initially saturated 0.8 m³ flows are then described and illustrated using representative frames and depth profiles. Next, velocity and volume fraction results are presented for volumes ranging between 0.2 and 1.0 m³ to illustrate the variation in flow behavior with source volume. Finally, laser scanning results of the deposit morphology of each trial are used to explore the nature of the relationship between travel angle and source volume for both dry and wet flows.

2. Experimental Setup and Methodology

The experiments consisted of a series of granular flows in a large indoor testing facility (Figure 2). The 2.09 m wide flume features a 8.23 m long section inclined 30° from horizontal and a 33 m long horizontal runout section. For the entirety of the inclined portion and for the first 3.68 m of the horizontal runout section, the base of the flume is constructed from bare aluminum and the side walls of the flume are glass to permit observation of the flows. Further down the flume, the base is constructed from smooth concrete. At the top, a release box with a hinged door can accommodate over 1.0 m³ of saturated material. The door was rapidly opened using pneumatic cylinders to initiate the experiment, with the door moving clear of the material within 0.4 s. At the completion of the test, the final deposit shape was surveyed using a Faro Focus S 150 Light Detection and Ranging (LiDAR) scanner from two or more scanning positions.

2.1. Video Capture and Instrumentation

During the test, a Phantom v2512 high-speed video camera was located near the end of the inclined portion of the flume (indicated as "CAM1" on Figure 2) to capture mature flow behavior in the travel stage. The camera was oriented in a side-on configuration to observe through the transparent glass side walls, rotated such that the width of the image was parallel to the base of the flume. The camera was set to capture a $1,280 \times 800$ pixel greyscale image at a frame rate of 7,500–10,000 fps (frames per second). A Tokina 100 mm f/2.8 Macro lens was used at its widest aperture to limit the depth of field and distinguish only the particles next to the glass side walls. The field of view was approximately 220 mm by 136 mm. A typical particle of 3.85 mm diameter was represented by a 23 pixel width in the resulting image.

As only one high-speed video camera was available, two initially saturated flows (0.4 and 0.8 m³ source volumes) were repeated with the same camera and lens situated within the horizontal portion of the flume ("CAM2" on Figure 2). At this location, the camera was situated further back from the sidewall. The field of view was approximately 285 by 178 mm, with a typical particle represented by 17 pixels.

Nine fluid pressure transducer sensors were installed into the base of the flume to quantify the basal fluid pressure (Figure 2). The sensors (TE Connectivity model U5244-000002-14BG, 0–140 mbar range, manufacturer's
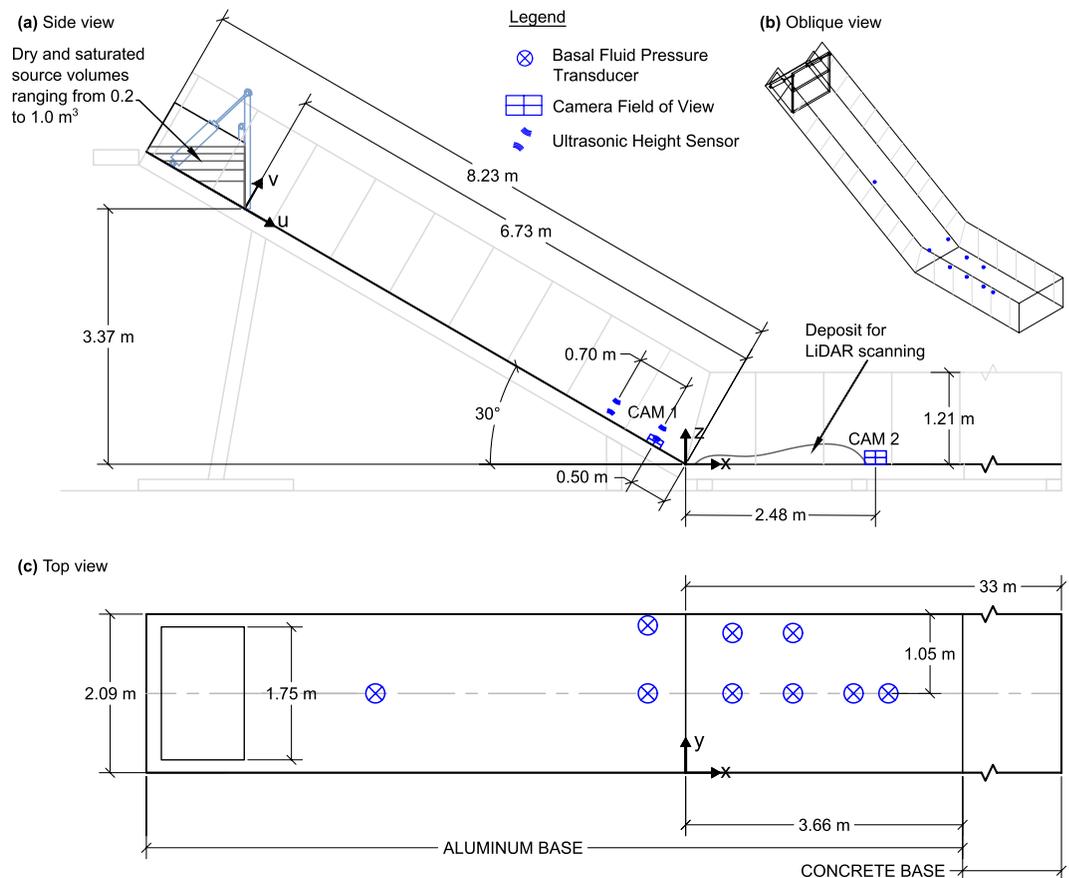
Figure 2. Diagram of (a) side profile, (b) oblique view, (c) top view of the experimental flume, illustrating the locations of high-speed video camera fields of view, basal fluid pressure transducers, and ultrasonic height sensors.

stated accuracy 7 mm, total error band 18 mm) were threaded directly into the flume. The fluid could enter each sensor through seven holes of 2 mm diameter.

Two ultrasonic distance sensors (model S18UUAQ, Banner Engineering Corp., 2.5 ms response time) were mounted above the inclined section of the flume, along the flume centerline (Figure 2). These sensors recorded the flow height away from the influence of the glass sidewalls by measuring the distance between the sensor and the top of the flow, normal to the flume base.

The sensor signals were sampled and recorded at 2,000 Hz. During the experiments, the pressure sensors were subject to noise considered to be resonance of the flume. The natural frequency of the flume structure was measured at approximately 140 Hz. To counteract this noise, the pressure sensor output signals were filtered using a 80 Hz low-pass Butterworth filter.

2.2. Materials and Preparation

Pseudo-spherical ceramic beads, manufactured by Saint-Gobain Norpro and marketed as Denstone 2000 Support Media, were used as the granular material for the experiments. These beads were chosen for their pseudospherical shape, relatively uniform diameter, and ability to be reused for multiple trials with minimal breakdown. The physical properties of a representative sample of 30 beads were measured and tabulated by Coombs et al. (2019). The beads were found to have an average diameter of 3.85 mm, grain sphericity of approximately 95%, and grain density of 2,241 kg m^{-3}. The bulk density was measured by Coombs (2018) as 1,400 kg m^{-3}, corresponding to a volume fraction of $\nu = 0.63$. According to the manufacturer, the hardness of the beads exceeds 6.5 on the Mohs scale. Triaxial tests conducted by Raymond (2002) gave effective friction angles of 33.7° at 20 kPa confining pressure.
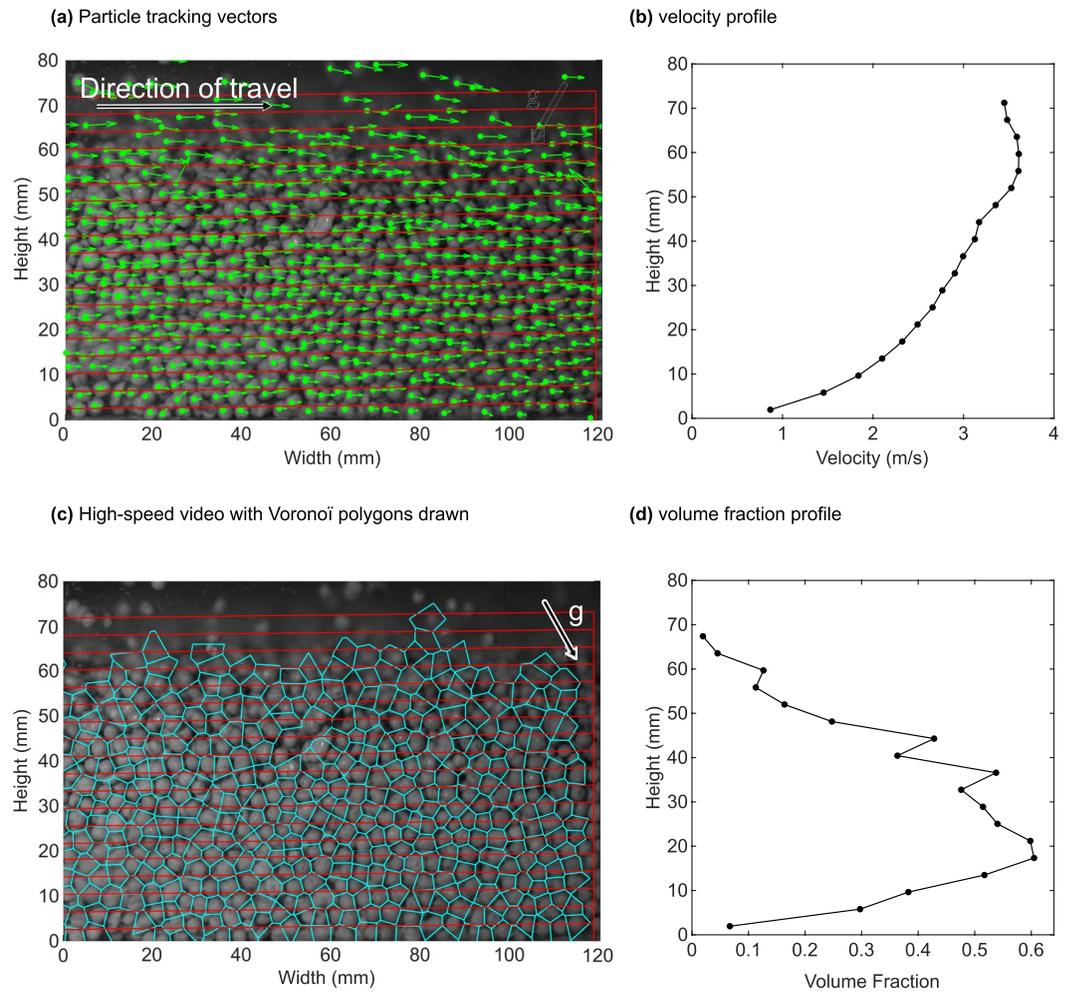
Figure 3. Representative video analysis and calculated profiles using PTV for 0.8 m^3 dry flow at peak flow height, illustrating (a) displacement vectors (green arrows) identified by PTV within bins drawn parallel to flume base (in red), (b) velocity profile calculated from displacement vectors within each bin, (c) Voronoï polygons drawn around particle locations for use in volume fraction estimation method, and (d) estimated volume fraction profile.

The source volumes tested were comprised of 0.2, 0.4, 0.6, 0.8, and 1.0 m^3. In each of the dry and initially saturated states, the material was made level in the release box using a rake. In the initially saturated state, the pore spaces were inundated with potable water at room temperature but ponding water on top of the beads was minimized. Chemical analysis of the tap water by Rowe et al. (2014) indicate concentration of key cations of 39 ppm (Ca), 9.5 ppm (Mg) and 18.6 ppm (Na).

3. High-Speed Video Analysis and Calculated Quantities

High-speed video was used to observe the flow structure and to provide images for further analysis. In this section, we discuss the image analysis methods used to identify the velocity and volume fraction for each test.

3.1. Particle Displacement and Velocity

The Particle Tracking Velocimetry (PTV) method involves first identifying the particle locations in selected frames and then using a PTV algorithm to link individual particles in successive frames (Brevis et al., 2010; Gollin et al., 2017; A. M. Taylor-Noonan et al., 2021). In our experiments, the camera is oriented to match the inclination of the flume base to optimize the field of view, for example, so the particle movement vectors (Figure 3a) are generally horizontal in the illustrations. The direction of gravity is noted on the figure.
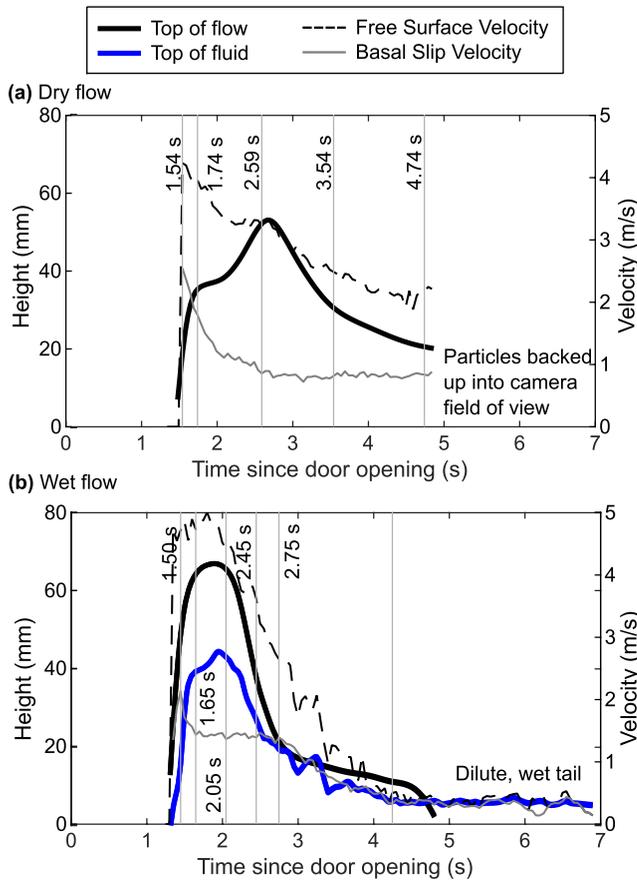
Figure 4. Flow heights (from side view camera) versus time, at "CAM1" location near the end of the inclined section of flume, for representative 0.8 m³ (a) dry and (b) wet flows. The initially saturated flow is taller, has the majority of the mass biased toward the front of the flow, and has a long thin tail portion. The top of fluid is below the top of flow at the time of peak flow height. The free surface and basal slip velocities are also shown.

The images were analyzed in sets of fifty (50) images. Each set was initiated at an interval of $t = 0.05$ s during the passage of the flow. Within each set, the frames were selected from the 7,500–10,000 fps video such that the analyzed frames were $\Delta t = 0.0004$ s apart (equivalent to 2,500 fps). For a particle moving at 5 m per second, the movement was 11.5 pixels and the resulting ratio of particle movement per frame to particle diameter was 0.52. For a particle moving at 1 m per second, the corresponding movement was 2.3 pixels. The results were grouped into bins (shown by red lines on Figure 3) to prepare depth profiles of the quantities, each drawn parallel to the flume base with height equal to one average particle diameter. Each vector was decomposed into components parallel (streamwise) and perpendicular to the flume base.

Velocity profiles (Figure 3b) were calculated by averaging the components of each vector located within the bin, for all pairs of frames that comprise the set. From the profile of streamwise velocity u, the shear strain rate with respect to depth is defined here by $\dot{\gamma} \equiv \partial u / \partial z$. This quantity indicates relative displacement within the flow. The velocity of the lowest bin, adjacent to the flume base, was considered to be the basal slip velocity. As an example, Figure 4 presents the free surface and basal slip velocities for representative 0.8 m³ dry and wet flows.

3.2. Volume Fraction

The volume fraction ν forms the basis for classification in Kinetic Theory and Extended Kinetic Theory (e.g., Chialvo et al., 2012; Jenkins, 2007; Lun, 1991). Randomly close packed spheres correspond to $\nu_{rcp} \approx 0.64$ (Allen & Thomas, 1999). Various contributors to Extended Kinetic Theory propose the frictional regime begins between $0.583 \leq \nu \leq 0.613$ when long-lasting particle contacts develop. Jenkins (2007) further divided the collisional regime into a "dense collisional" regime ($0.49 < \nu \leq 0.583$) and "dilute collisional" regime ($\nu \leq 0.60$) based on a change in the likelihood of a particle collision. This proposed classification has been shown in the background of volume fraction plots in the following sections.

To estimate volume fraction ν, the image plane is first divided into Voronoï polygons, each containing one identified particle centroid location (Figure 3c) and drawn such that all points in the polygon are closer to that identified particle than any other. Then, ν is estimated using two methods proposed by Capart et al. (2002), which consider the size and shape of Voronoï polygons as the basis of estimation. Both methods were developed for the case where particles are observed against a rigid transparent wall, but calibrated with the average volume fraction in the cell and are thus expected to estimate the volume fraction away from the influence of the rigid wall.

Only the area of the polygons is considered for relatively dilute flows ($\nu \leq 0.20$). For $\nu > 0.20$, the shape of the polygons is considered using a roundness parameter $\xi = 4\pi A/P^2$ where A and P are the area and perimeter of the Voronoï polygon around the particle, respectively. The roundness parameter ξ is calculated for all the particles in a bin over all the frames in each set. Voronoï polygons which share an edge with the analysis area of interest were disregarded, as the shape of these polygons may have been clipped by the analysis area of interest. Before inclusion into the average, each Voronoï polygon was assessed for size and shape; Voronoï polygons with areas exceeding 2.5 times the area of an average particle or with a roundness parameter ξ below 0.70 were then discarded, and any polygon bordering these discarded polygons were withheld from the average. Once the average ξ is calculated, the volume fraction profile (Figure 3d) is estimated by:

$$\frac{\nu}{\nu_{rcp}} = \left(\frac{\xi - \xi_0}{\xi_{rcp} - \xi_0} \right)^{\beta} \tag{1}$$

For random close packing of spheres, $\nu_{rcp} \approx 0.64$ (Allen & Thomas, 1999). Capart et al. performed a calibration study for volume fractions in the range $0.20 \le \nu \le 0.55$ and found calibration constants $\xi_{rcp} = 0.84$, $\xi_0 = 0.72$, and $\beta = 3.5$.

As the flow inevitably contained some saltating particles above the flow, a threshold is required to define what is considered to be the body of the flow. For the purposes of further analysis and discussion in this paper, the flow height of the trials was set by the threshold $\nu = 0.20$ over height and time (Figure 4). Some manual adjustments were made to exclude particles which were not immediately beside the sidewall glass. This was judged by the shallow depth of field of the camera lens and the incident light. The top of fluid was manually marked on images at 0.05 s intervals for the wet flows.

4. Flow Characteristics

We begin the comparison of dry and saturated flows through visual observations of flow structure, velocity, volume fraction, and pore pressure measured at the observation point near the end of the inclined section of the flume (the "CAM1" location). The times examined are shown on Figure 4. The 0.8 m³ volume is chosen for this comparison of typical anatomy of the flows as this source volume exhibits the system of flow regimes discussed throughout this paper but is not at the extreme of source volumes tested. Later sections of the manuscript explore the variability observed in larger and smaller volumes and full analysis of the resulting deposit morphology.

4.1. Dry Flow

The flow regimes within a 0.8 m³ dry flow are revealed by the velocity and volume fraction profiles as it passes the "CAM1" location (Figure 5) at selected times t since door opening. The initial front of the granular flow is heralded by saltating particles (Figure 5a) with $\nu \approx 0.2$ and basal slip velocity in excess of 2.5 ms⁻¹. A high level of collisional activity is seen when reviewing the video. Later at $t = 1.74$ s (Figure 5b), the volume fraction increases to approximately $\nu = 0.27$. The bottom of the flow slows and the shear strain rate $\dot{\gamma}$ quickly increases. The basal slip velocity is 1.8 ms⁻¹, while the surface velocity is 4.0 ms⁻¹ with a flow height of 36 mm.

The peak flow height comprises a dense ($\nu > 0.49$) core above a collisional base with a higher magnitude of $\dot{\gamma}$. The peak flow height of approximately 52 mm is visible at $t = 2.59$ s (Figure 5c). The surface velocity is approximately 3.4 ms⁻¹, slower than at $t = 1.74$ s even though the flow height is higher. The basal slip velocity has reduced further to approximately 0.9 m s⁻¹.

At $t = 4.74$ s (Figure 5e), the flow height has reduced to approximately 21 mm and ν has reduced to approximately 0.43. The basal slip velocity remains at 0.8 ms⁻¹ and the surface velocity has reduced to 2.2 ms⁻¹. At $t = 4.85$ s, the determination of the velocity for the 0.8 m³ flow is not possible as particles at rest begin to back up into the camera's field of view. The runout morphology for this experiment is discussed in Section 6.
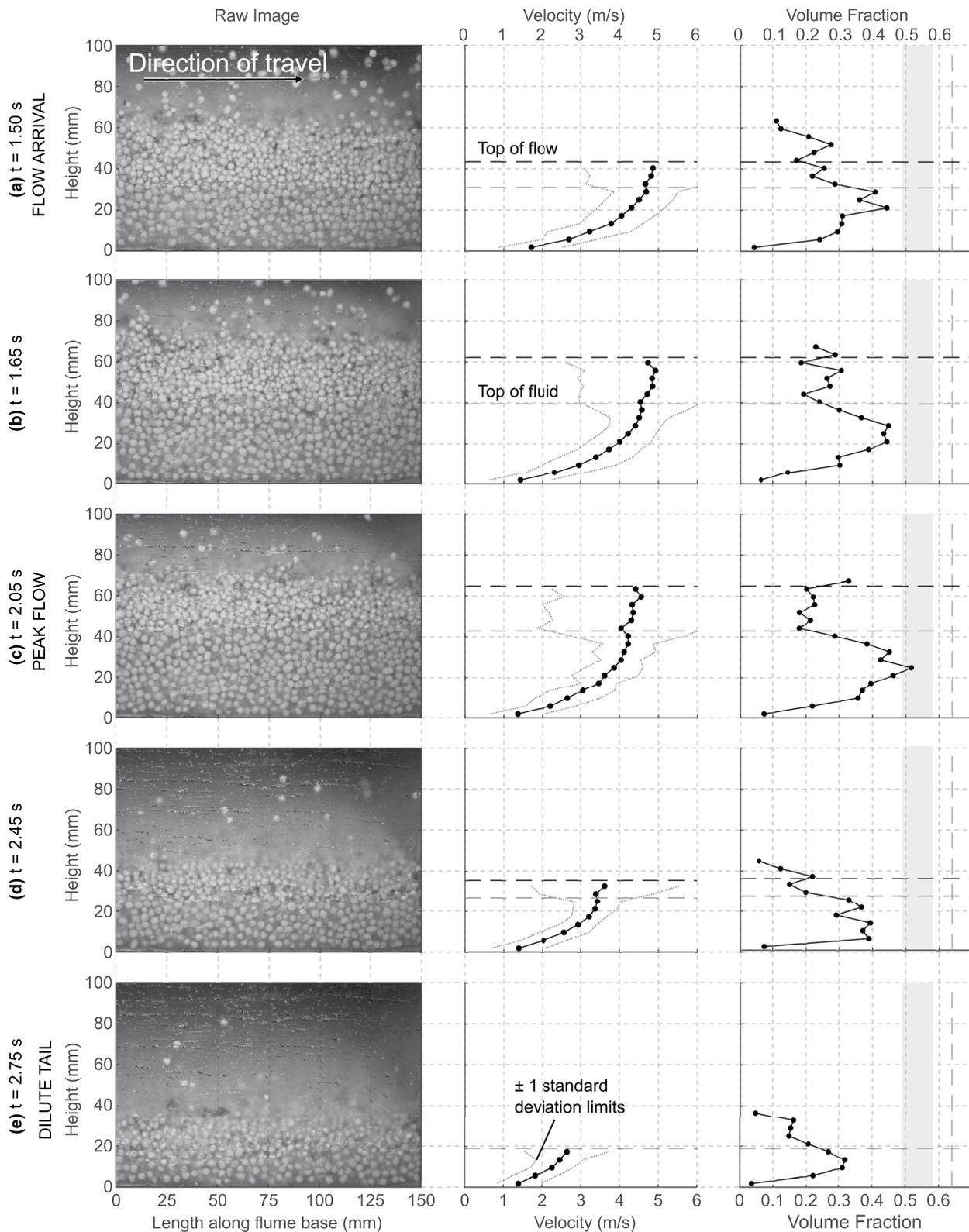
4.2. Saturated Flow

The typical behavior of a fluid saturated flow is presented in Figure 6 for the 0.8 m³ volume. The front of the flow arrives before the fluid, similar to the unsaturated granular front observed in laboratory experiments by Leonardi et al. (2015) and Turnbull et al. (2015). In the early arrival stages of the core of the flow (Figure 6a), the top of fluid is seen at an approximate height of 30 mm while the flow height is approximately 43 mm. The free surface velocity exceeds 4.8 ms⁻¹, faster than the dry flow. The velocity profile shows a very high $\dot{\gamma} \approx 200$ s⁻¹ near the flume base and minimal $\dot{\gamma}$ above the top of fluid. In rigid bed experiments, Armanini et al. (2005) also measured the highest $\dot{\gamma}$ near the base. Here, the flow is dilute, with identified volume fractions typically ranging between 0.3 and 0.4.

By $t = 2.05$ s, the flow height and the top of fluid are at their peak (Figure 6c), while the surface velocity has decreased to 4.5 ms⁻¹. The concentration of shear near the base of the flow continues. The density is less than the dry flow and is further reduced near the top of flow. Below the top of fluid, the maximum volume fraction is $\nu = 0.52$. In the portion of the flow above this, $\nu = 0.21$.

The top of fluid is coincident with the surface at $t = 2.75$ s (Figure 6e) as the tail of the flow passes 'CAM1'. The flow is relatively dilute with $\nu = 0.32$. The basal slip velocity reduces from 1.6 ms⁻¹ at $t = 2.75$ s to 0.4 ms⁻¹
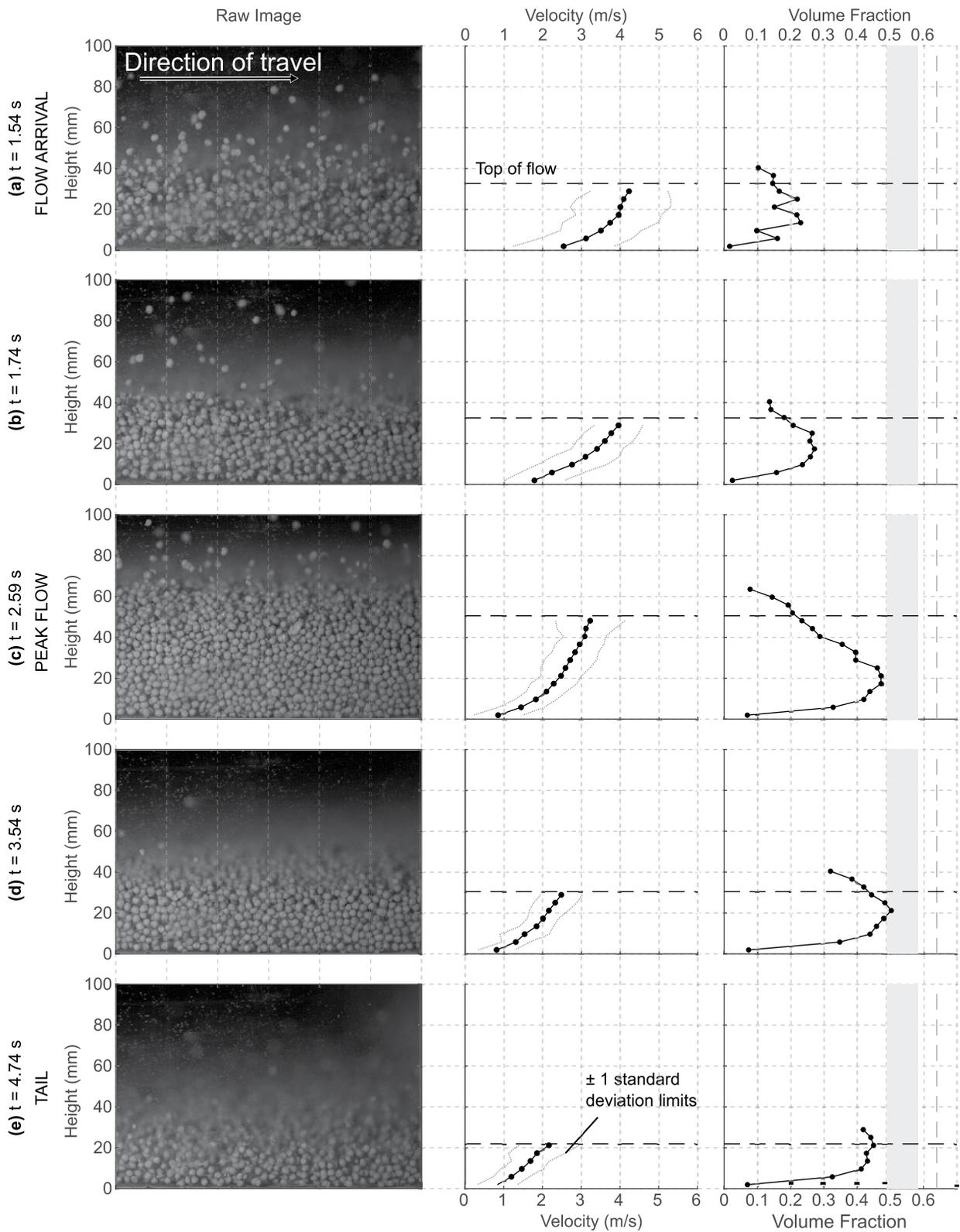
Figure 5. Anatomy of 0.8 m³ dry flow at end of inclined section of flume ("CAM1"), showing a frame of video, the velocity profile with ±1 standard deviation limits (in the 0.02 s observation time window), and the volume fraction ν at times (a) $t = 1.54$ s, (b) $t = 1.74$ s, (c) $t = 2.59$ s, (d) $t = 3.54$ s, (e) $t = 4.74$ s since door opening.

Figure 6. Anatomy of 0.8 m³ initially saturated flow at end of inclined section of flume ('CAM1') showing a frame of video, the velocity profile with ±1 standard deviation limits (in the 0.02 s observation time window), and the volume fraction ν at times (a) $t = 1.50$ s, (b) $t = 1.65$ s, (c) $t = 2.05$ s, (d) $t = 2.45$ s, (e) $t = 2.75$ s since door opening. The shading in the volume fraction plot represents the dense collisional regime ($0.49 \leq \nu \leq 0.583$).

at $t = 4.00$ s, at which time the flow is only two particles high. This is in stark contrast to the tail end of the dry flows, where the basal slip velocity is seen to be relatively constant (Figure 4).

Overall, the partitioning into a head section, frictional core, collisional base, and tail section is more pronounced for a wet flow then dry flow of the same volume.

A similar, repeat, test was carried out for the 0.8 m³ initially saturated flow, with the high-speed video camera set at the "CAM2" location (Figure 2) on the horizontal runout portion of the flume. The results show that the flow arrives in a dense ($\nu > 0.49$) state with only a thin film of water around the particles, with a free surface speed of approximately 2.6 ms⁻¹ (Figure 7a), which is approximately half that at the time of peak flow at the upstream "CAM1" position. The peak flow height is over 100 mm, approximately two-thirds greater than at "CAM1." This shows that the material has laterally compressed following the change in slope. $\dot{\gamma}$ is highest near the base.

The top of fluid rises quickly to 102 mm above the flume base at $t = 2.40$ s (Figure 7b). A reduction in the volume fraction occurs simultaneously, especially near the top of the flow. The velocity decreases throughout the depth profile after the peak flow height passes (Figure 7c at $t = 3.00$ s). The density increases in the lower portion of the flow. Later, the flow arrests completely while the tail is in the view of the camera.

4.3. Basal Fluid Pressures

During the initially saturated 0.8 m³ flow, the centerline and side basal fluid pressure sensors at $x = -0.50$ m show similar peak pressure measurements. This leads to the conclusion that the flow is sufficiently mature at "CAM1" to have recovered from the initial impulse of the granular collapse from the source box. Further down the flume at $x = +1.42$ m, the pressure traces are also generally similar from the centerline location to the side location (Figure S1 in Supporting Information S1).

The visually identified top of fluid at the side of the flow can be compared to the measured basal fluid pressure P_f at the center of the flow, expressed as an equivalent bed-normal fluid height $H_f = P_f/\rho_w g \cos\theta$, where the density of water $\rho_w = 1{,}000$ kg · m³, the slope angle $\theta = 30°$ and $g = 9.81$ m · s⁻². Here, the height H is similar between the visually identified flow height (at the side wall) to the ultrasonic flow height sensor (at the centerline). The equivalent height of the basal fluid pressure is equal to the height of the fluid, indicating that the matrix fluid pressures did not exceed the hydrostatic regime.

The basal fluid pressures consistently increase across the four sensors installed on the horizontal runout portion. The highest pressures observed are at the furthest distance from the release box. This is attributed to the increasing flow height as the front of the flow slows and the rear of the flow cascades over. Good agreement is seen between the equivalent fluid height from the sensor at $x = +2.68$ m and the top of fluid. The wet flow is subject to contraction during the arrest phase but the basal fluid pressures do not increase above hydrostatic.

5. Effect of Varying Source Volume

In this section, we expand on the comparison of dry and initially saturated flows using observations of flow thickness, velocity, volume fraction, and pore pressure measured at the observation point near the end of the inclined section of the flume (the 'CAM1' location) for source volumes ranging between 0.2 and 1.0 m³. This comparison is conducted to look at the flow structure over the depth of each flow at each volume, and noting any differences that may give rise to scale effects with flow volume.

5.1. Flow Thicknesses and Fluid Pressures

As source volume increased through the tested range of 0.2–1.0 m³, the observed maximum flow thickness at $x = -0.50$ m ("CAM1") increased from 38 to 51 mm for the dry flows and from 30 to 79 mm for the initially saturated flows.

As shown in Figure 8 at $x = -0.50$ m, the maximum equivalent bed-normal fluid height (as calculated in Section 4.3) is equal to the peak flow height for the range of initially saturated source volumes tested. This suggests the matrix fluid pressures did not exceed the equivalent hydrostatic regime. The pore pressure ratio r_u, defined here as the ratio of fluid pressure to the total vertical pressure, ranges between [0.36:0.44].
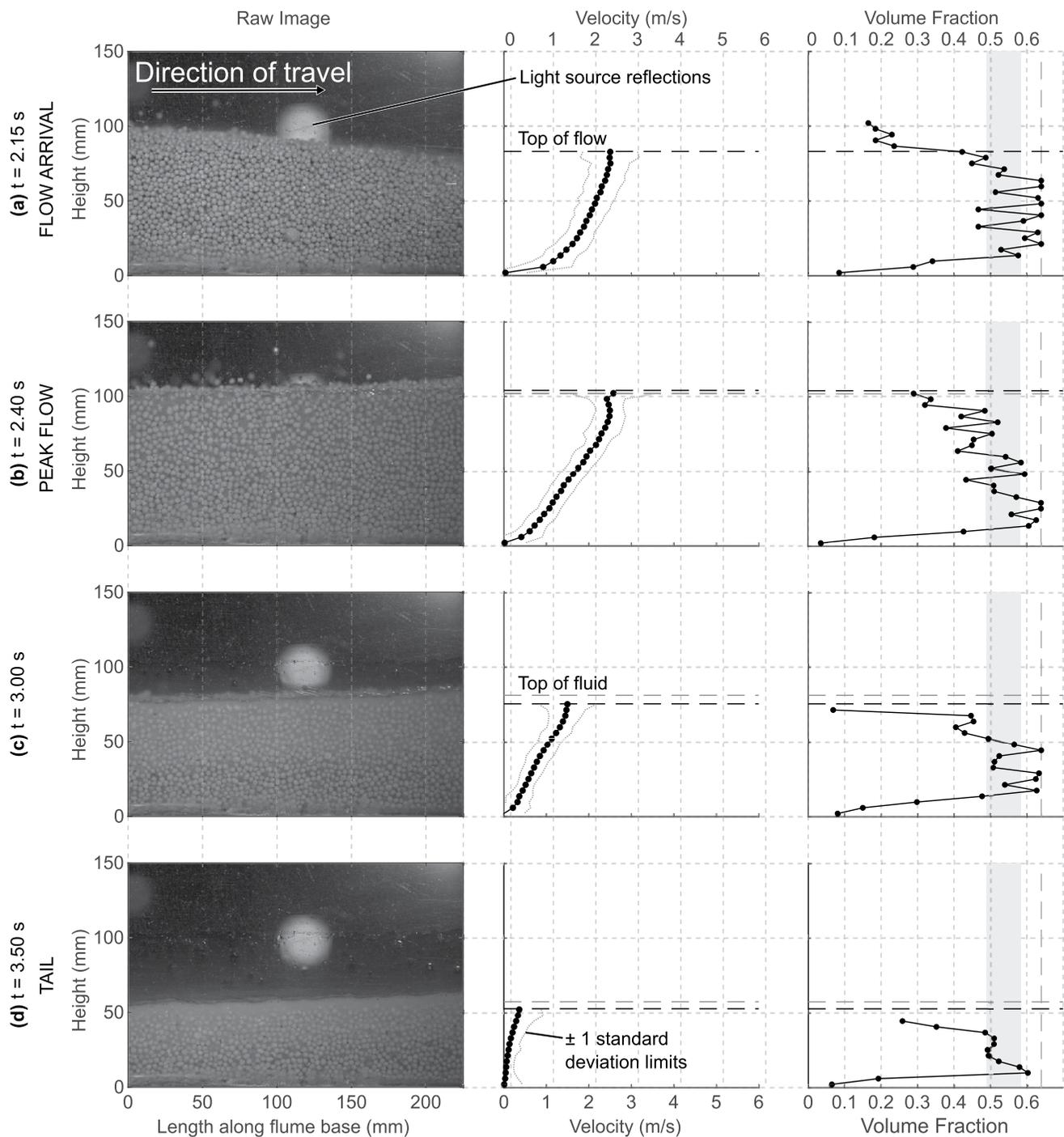
Figure 7. Anatomy of 0.8 m³ wet flow in horizontal runout section of flume ('CAM2') showing a frame of video, the velocity profile with ±1 standard deviation limits (in the 0.02 s observation time window), and the volume fraction ν at times (a) $t = 2.15$ s, (b) $t = 2.40$ s, (c) $t = 3.00$ s, (d) $t = 3.50$ s since door opening. The shading in the volume fraction plot represents the dense collisional regime ($0.49 \leq \nu \leq 0.583$).

5.2. Behavior at Peak Flow Height

In Figure 9, the time of peak flow height passing "CAM1" is selected as a basis for comparison between the flows. This is the time when the flow is at its thickest and most dense state, and therefore the transport rate of mass is highest. A review of the profiles, discussed in detail below, provides information on the state of flow at
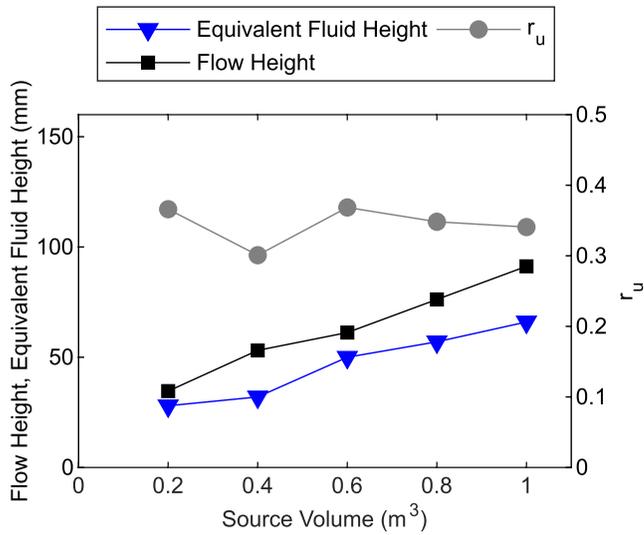
Figure 8. Peak flow heights and fluid pressures observed at $x = -0.50$ m along centerline for initially saturated trials, with equivalent fluid height remaining below flow height over range of source volumes tested. The pore pressure ratio r_u is defined here as the ratio of fluid pressure to the total vertical pressure.

the end of the incline as well as the partitioning of particles between highly shearing, lightly shearing, and collisional regimes.

At the time of peak flow height passing "CAM1," the velocity profile of each of the initially saturated flows ("wet") is faster than that of the dry flows. The overall velocity of the wet flows increases as source volume increases, with the top of the core of the 1.0 m³ flow attaining a speed exceeding 5.0 ms⁻¹. The opposite is noted for the dry flows, which are seen to be slower for each height in the flow as source volume increases. Wet flows of all volumes are each seen to have a very high $\dot{\gamma}$ near the base of the flow. The shape of the velocity profiles normalized for both height and velocity (Figure 10) are similar throughout the source volumes for each state (dry or wet). In Section 7, these normalized shapes will be compared to theoretical velocity profiles, published experimental results, and published velocity profiles of natural flows.

At "CAM2" after the change in slope, the 0.8 m³ wet flow maintains this highly shearing flow which transports material above the top of fluid to the front of the flow. By comparison, the 0.4 m³ wet flow displays minimal shearing at the same location.

Across the range of source volumes, the volume fraction profiles at the time of peak height passing "CAM1" (Figure 9) for the dry flows display a similar shape as the 0.8 m³ flow discussed above. The maximum volume fraction of the core increases with source volume. Each volume of wet flows displays a similar shape as the 0.8 m³ flow, with a reduction in volume fraction above the top of fluid. The 0.2 through 0.6 m³ dry flows each are entirely in a collisional regime when assessed by volume fraction. The 0.8 and 1.0 m³ dry flows each have portions exceeding $\nu = 0.583$, indicating a frictional regime. While the maximum volume fractions of the wet flows increase slightly with source volume, the wet flows each have a lower maximum volume fraction than the dry flows of the same source volume and all remain in a collisional regime. For the dry flows, the volume fraction near the base is relatively consistent over the range of 0.2–0.8 m³. For the 1.0 m³ flow, the dense region is seen to extend down to near the flume base, suggesting that the increased confining pressure of the thicker frictional core has suppressed the collisional base. The wet flows displayed a reduction in volume fraction near the base over the range of source volumes, coincident with a high $\dot{\gamma}$.

5.3. Longitudinal Distribution of Regimes

We note that the core region of the initially saturated flows appears to enter an efficient mode of transport that increases in velocity with source volume, that is, for the larger source volume trials the velocity at each height in the flow is faster than the same height the smaller source volume trials (Figure 9). Hence, the volume of this core region relative to the total flow volume is examined here. The partitioning into regimes along the length of the flow from head to tail can be assessed through plots of the measured quantities for each analysis interval and depth bin. Figure 11 shows the volume fraction results and Figure 12 shows the velocity results in a contour plot format where the contour lines represent isovelocity lines. $\dot{\gamma}$ can be inferred from the vertical distance between the isovelocity contour lines: isovelocity lines closer together represent a higher shear rate. Where the lines are parallel to the x-axis, that portion of the velocity profile is constant with time.

The volume fraction of the dry flows (Figure 11) shows partitioning of the flow into a dilute, saltating head preceding the front, a dense core where volume fraction increases with source volume, and a gradual reduction of volume fraction toward the tail. During this transition period, the velocity results show only gradual changes with time (Figure 12). Geometric similarity of the flow height over time is evident across the range of source volumes and the change in flow height between core and tail is gradual. In contrast, for the wet flows the regime of the tail is distinct from the core for the volume fraction and velocity fields (Figures 11 and 12, respectively).

The initially saturated flows each display a period with near-constant velocity in the base of the flow (Figure 12), with the duration of this increasing with source volume. Only a short period of near-constant velocity in the base is observed within the 0.2 m³ flow, increasing to 0.9 s for the 1.0 m³ flow. The maximum $\dot{\gamma}$ near the base does not
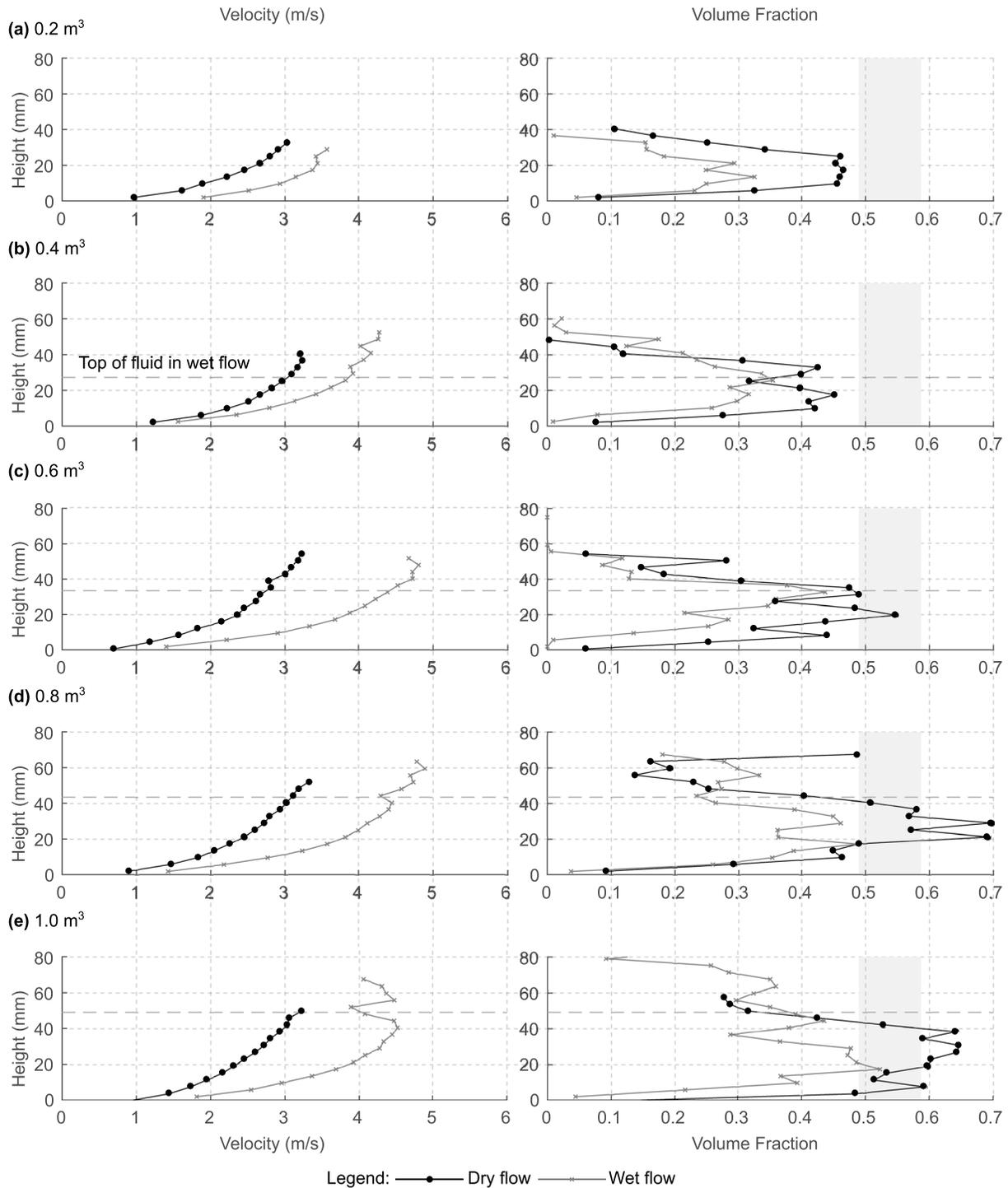
Figure 9. Comparison of depth profiles of streamwise velocity and volume fraction at the time of maximum flow height for (a) 0.2 m³ to (e) 1.0 m³ flows in 0.2 m³ increments. The shading in the volume fraction plot represents the dense collisional regime ($0.49 \leq \nu \leq 0.583$).

vary significantly with source volume, suggesting that the wet flows find a preferred, efficient state of flow. The velocity profiles remain near-constant as the flow height reduces until seemingly falling below a critical threshold where the velocity abruptly reduces and the tail begins. This behavior is also visible on a plot of the basal slip velocity over time from the flow front (Figure 13) as a distinct period of near-constant basal slip velocity for the wet flows but not for the dry flows.
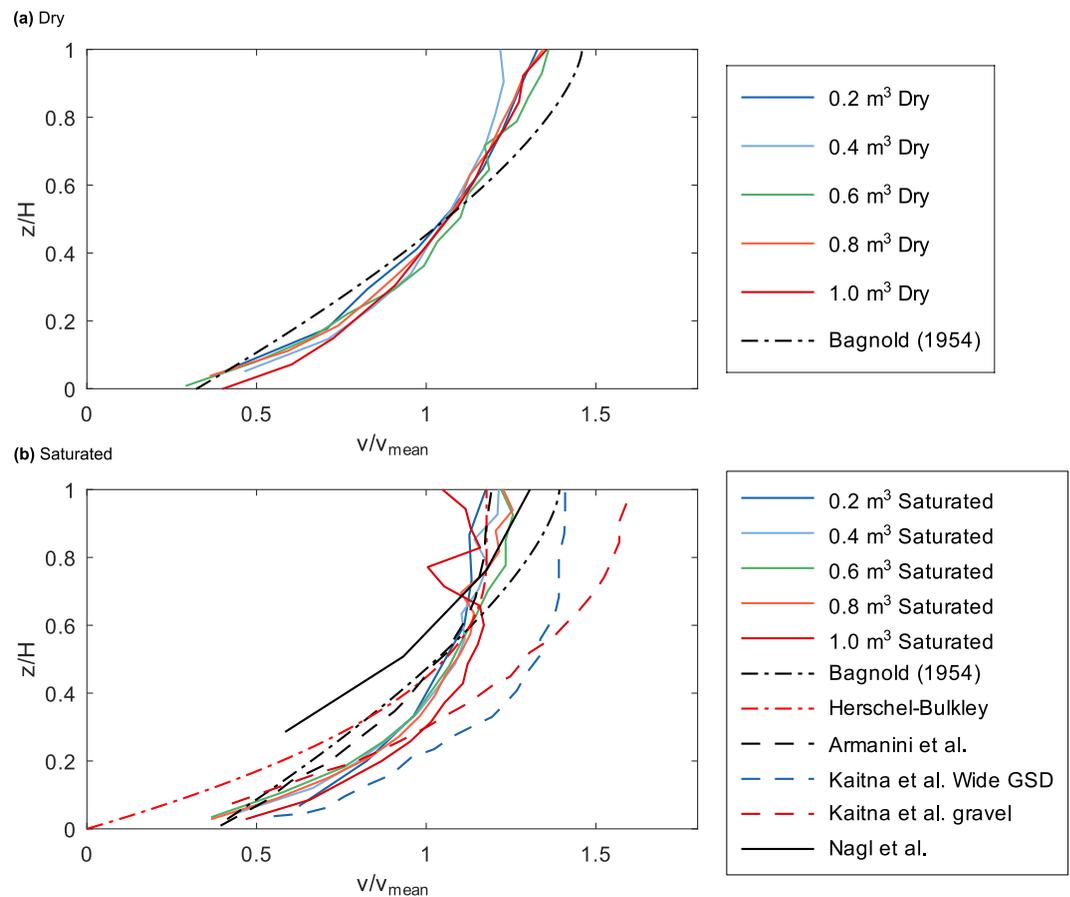
Figure 10. Normalized velocity profiles for (a) dry and (b) wet flows compared with Bagnold (1954) and Herschel-Bulkley velocity profile. Wet flows in (b) compared with steady-state laboratory results of Armanini et al. (2005) for wet flows on a solid bed and Kaitna et al. (2014) for wet flows in a rotating drum, as well as field data of Nagl et al. (2020) (for peak flow height).

The decrease in velocity from core to tail was greater for the wet flows than the dry flows. An effect for the deceleration of the wet flows is thought to be due to surface tension between the liquid phase with the flume base and sidewalls. At this stage, the tail portions of the initially saturated flows are slow moving and of low volume fraction and minimal thickness. Some ceramic beads remained on the flume surface at the end of the experiments until the remnant water evaporated. The material partitioned to this slow-moving tail would reduce the volume available to be transported at high speed in the core section of the flow. This is in accordance with the description of 'starving' avalanches by Bartelt et al. (2007).

6. Variation of Morphology of Resultant Deposit With Source Volume

In the previous section, observations at the grain-scale revealed localized shearing at the base and evolution of volume fraction zones with flow height. In this section, we explore the changes in bulk behavior, as reflected in the deposit morphology, for the varied source volumes.

The deposit morphology for each of the five dry and five saturated flow volumes, captured using LIDAR scanning, is presented in Figure 14. The profile of deposit morphology illustrates geometrical similarity (center-of-mass travel distance, shape and slope angle of the deposit) over the range of source volumes for dry flows. In contrast, the initially saturated flows display markedly increased runout distances as source volume increases. Runout statistics, illustrated schematically in Figure 1a, can be used to summarize the resultant deposit morphologies (Figure 15). The frontal extents of the flow are considered in Heim's Ratio H/L (Figure 15a). Heim's Ratio
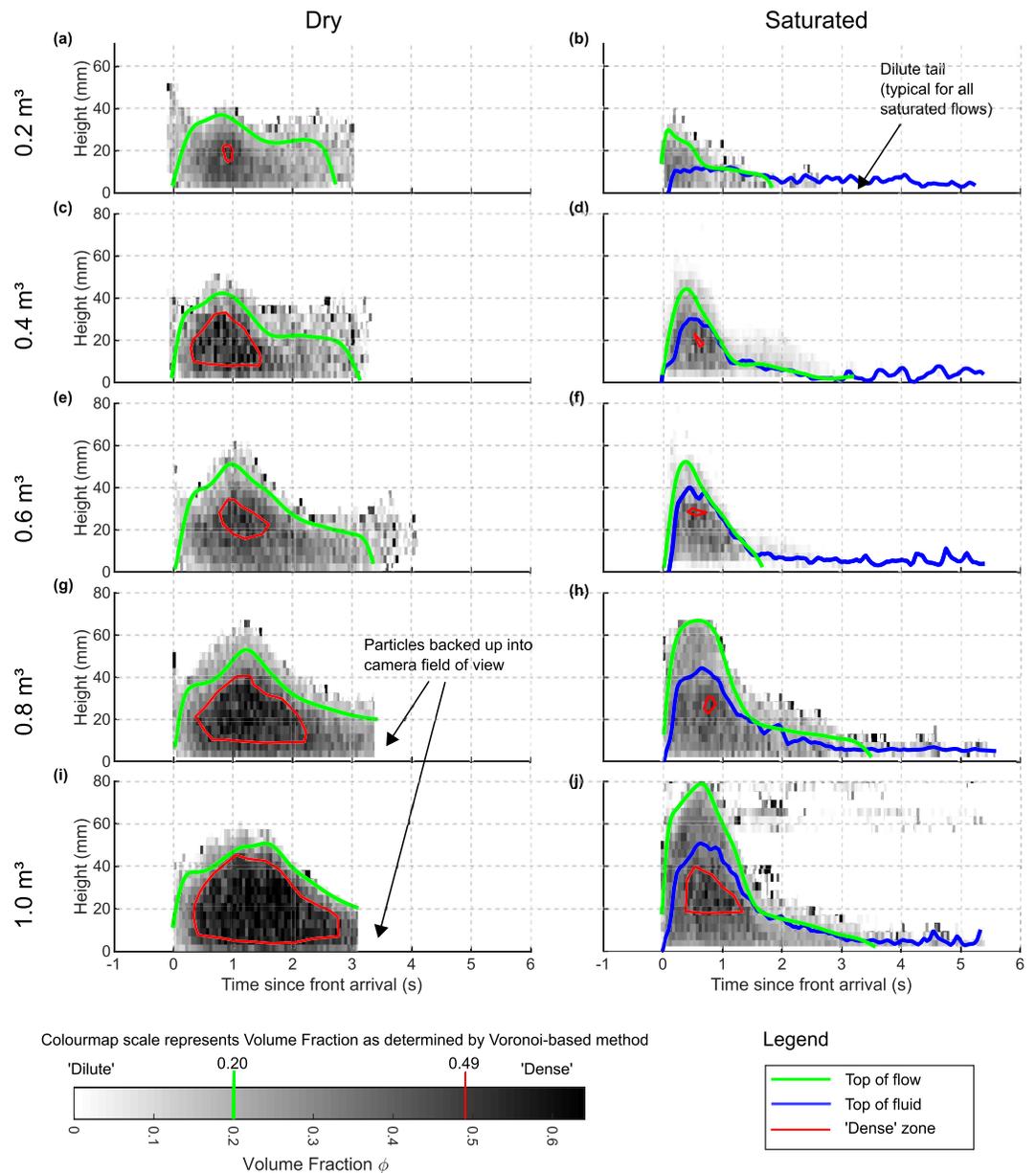
Figure 11. Height (*y*)-Time (*x*)-Volume Fraction (color scale) plots for dry and saturated trials over the range of source volumes, illustrating the formation of a dense granular core for dry flows and a comparatively dilute core for wet flows. Both flows exhibit a reduction in volume fraction near the rigid flume base.

remains relatively constant for dry flows but decreases significantly for initially saturated flows, indicating increased mobility with volume.

The travel angle statistics summarize the translation of the center-of-mass (Figure 15d), with a lower travel angle indicating a general increase in mobility. For the dry tests, a relatively consistent travel angle of 27.1°–28.1° was calculated over the range of source volumes tested. For the wet tests, the travel angle reduced significantly from 25.7° for a source volume of 0.2 m³ to 20.1° for a source volume of 1.0 m³. This marked decrease indicates that one or more physical processes within the rheology of the wet flows are affected by experiment size.
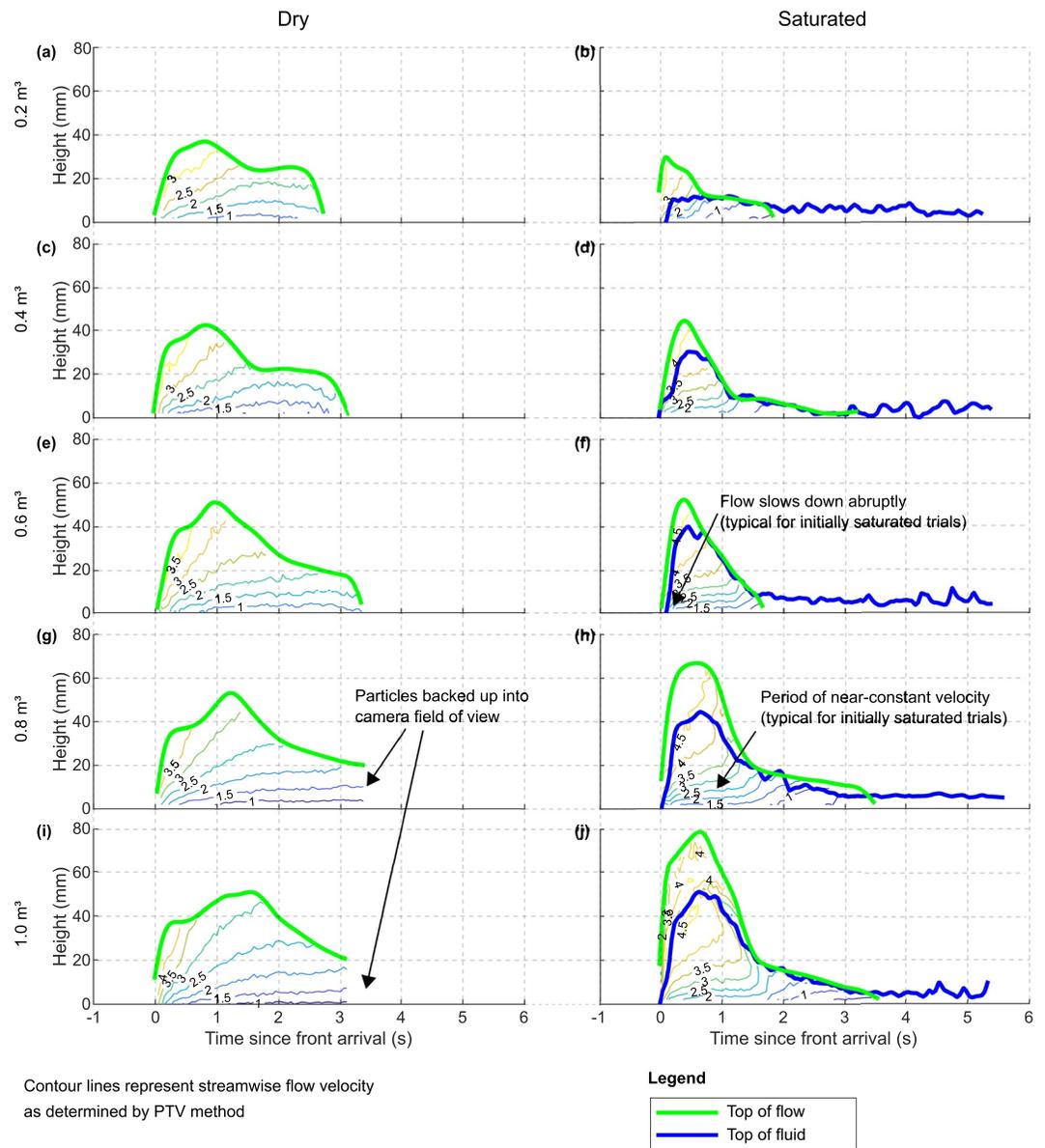
Figure 12. Height (y)-Time (x)-Velocity (color scale) plots for dry and initially saturated trials over the range of source volumes, illustrating a period of near-constant velocity near the base of the flume for the initially saturated state, suggesting that the flows find a preferred, efficient state of flow for translation and until the core height reduces below a critical threshold.

7. Discussion

In this discussion, we first look at the relative contributions of sliding and spreading to the runout distance results. We then briefly explore the fit quality of both a granular and non-Newtonian fluid flow model to the velocity profile results at each flow volume. Finally, we place our experiments in context with other laboratory and outdoor flows through non-dimensional numbers and velocity profile results.

7.1. Contributions to Extended Runout Distances

Parez and Aharonov ([2015](#)) proposed a general decomposition of flow runout distance where the total runout length L includes translation L_{COM} and forward spreading S_f. Parez and Aharonov further proposed a model for
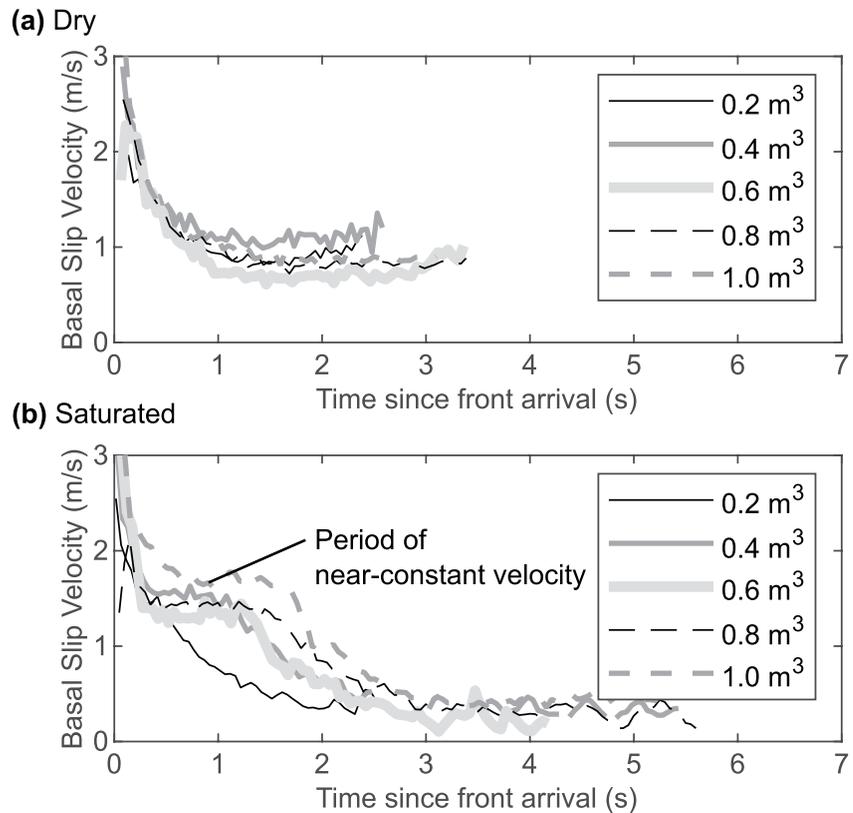
Figure 13. Comparison of basal slip velocities at end of the inclined surface for (a) dry trials illustrating the gradual decline in basal slip velocity and (b) initially saturated trials, illustrating a "step" phenomenon where the velocity remains constant while the core passes, then quickly reduces to a slow speed (<0.5 ms^{-1}) for the tail.

dry flows with a sliding term independent of source volume V (first term on the right hand side) and spreading term dependent on source volume (second term on the right hand side):

$$L = \frac{H}{\mu_0} + \left(\frac{3}{\pi \tan \alpha_{thr}} V \right)^{1/3} \tag{2}$$

In the translation term, Parez and Aharonov define μ_0 as the bulk flow resistance. For dry flows, μ_0 is a material parameter and not dependent on source volume. Recall from Figure 1 that $L = R_i + L_{COM} + S_f$, where R_i is the distance between the rear extent and the center of mass of the source volume. In the above equation, is it assumed that $R_i + L_{COM} \approx (H - H_{COM}) / \mu_0 + H_{COM} / \mu_0 = H / \mu_0$ and the equation is presented in terms of the overall H and L and not L_{COM}, H_{COM}, and R_i. In the spreading term, the model assumes the deposition area is not laterally constrained and the deposit forms a cone shape with final side slope angle α_{thr}. Thus, $S_f^3 \propto V$.

While the Parez and Aharonov model was developed for dry flows, we use the decomposition concept (runout as the sum of translation and spreading terms) here to look at the relative contributions of each. Further, we use the form of Equation 2 to estimate bulk flow resistance μ_0 which is related to the travel angle α_g (Figure 15d) by $\mu_0 \approx H_{COM}/L_{COM} = \alpha_g$.

First, for the translation term, the relatively constant travel angle of dry flows (Figure 15d) is in agreement with the Parez and Aharanov model. For wet flows, the declining travel angle with source volume is evidence that the reduction in flow resistance is not simply due particle buoyancy and the corresponding reduction in geotechnical effective stress, as this would still result in a constant μ_0. The behavior observed does not require the presence of excess pore pressure.

The deposit shapes of both the dry and wet flows display general geometric similitude upon initial inspection (Figure 14), which is a key assumption of the second term of Equation 2. The spreading distance S_f can be seen in
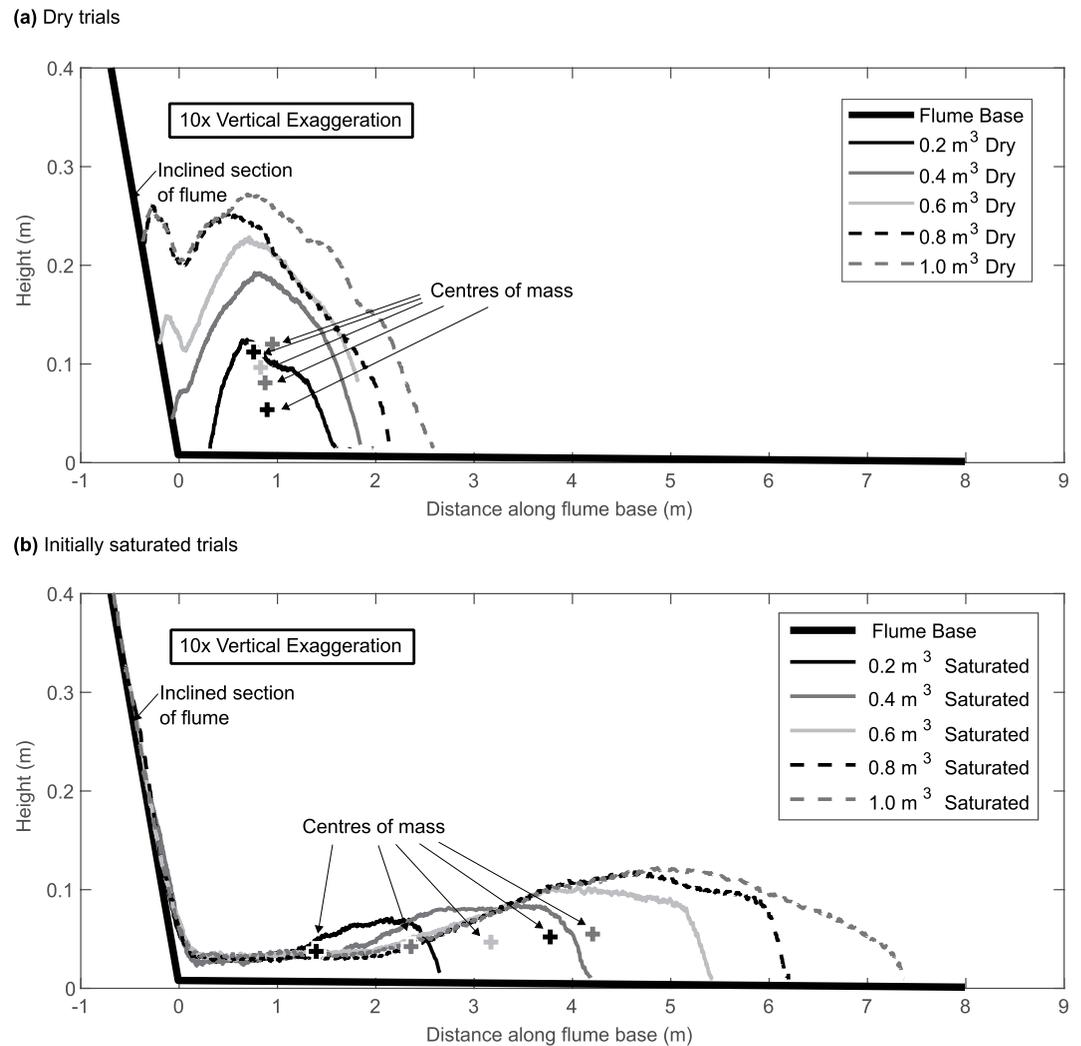
Figure 14. Comparison of resultant deposit morphology profiles for (a) dry and (b) initially saturated trials, with calculated centers of mass indicated.

the statistics of the runout (Figure 15b) as the distance between the positions of the center-of-mass and the flow front. Here, we are comparing to a flume where the sidewalls laterally constrain the flow and the flow could only spread in one direction. The height also would increase proportionally to S_f based on geometric similitude. From this, $V \propto S_f^2$. Accordingly, the ratio S_f/V^2 is presented in Figure 15c. A constant value of S_f^2/V implies that the spreading term is scaling in the form similar to that assumed in the second term of Equation 2. The normalized spreading distances S_f^2/V were higher for wet flows than dry, following from the shallower side slope angles of the deposits. A review of the relationship of S_f^2/V over the range of flow volumes reveals a near-constant value for the dry flows, but S_f^2/V shows a slight increase with flow volume for the wet flows. This may be due to fluid drag as the interstitial fluid exits the matrix of slowing particles. However, the increase is slight and translation, rather than spreading, was the strongest contributor to the increase in runout length with source volume for wet flows.

7.2. Comparison With Published Velocity Profiles

In order to assess the flow behavior of our experimental flows we fit two flow models to the normalized measured velocity profiles (Figure 10). The first is in the form of Bagnold (1954), representing a dry granular flow:

$$u(y) = a\left[h^{3/2} - (h-y)^{3/2}\right] + b \tag{3}$$
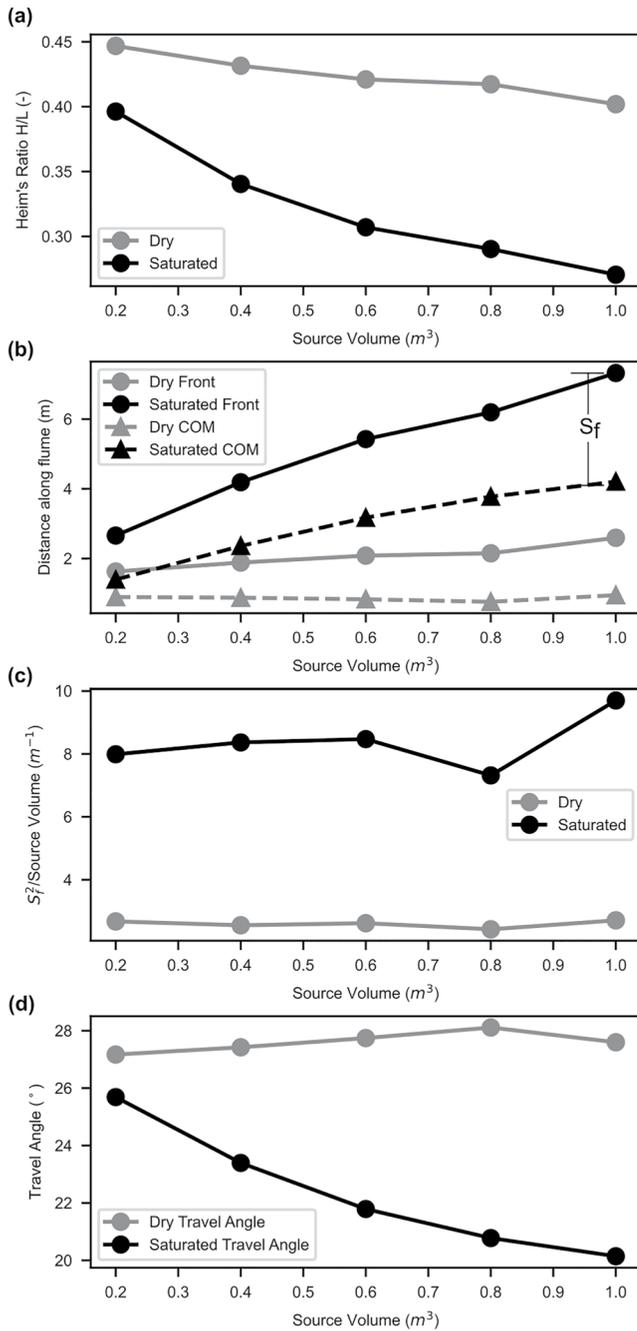
Figure 15. Comparison of summary statistics of mobility, showing (a) Heim's ratio from top of source volume to distal reach of deposit, (b) position of front extent of deposit and center-of-mass of deposit, illustrating the relative contributions of each to total runout, (c) possible scaling relationship of S_f with source volume and (d) travel angle between centers of mass.

where h is the flow height and a, b are best-fit constants corresponding to velocity scaling and basal slip velocity, respectively.

The Inertial Number I is defined for a dry granular flow describing the relative importance of inertia and confining stresses (GDR MiDi, 2004). A higher magnitude of I is associated with a more collisional flow. By GDR MiDi (2004),

$$I = \frac{\dot{\gamma} d_p}{\sqrt{P/\rho_s}} \tag{4}$$

where $\dot{\gamma}$ is the local shear strain rate, d_p is the characteristic particle diameter, P is the total stress at the depth for which I is to be calculated, and ρ_s is the particle solid density.

The velocity profile of Equation 3 leads to a constant Inertial Number (Equation 4) throughout the flow height, and this is expected for dense granular flows following the $\mu(I)$ rheology (Forterre & Pouliquen, 2008).

The velocity profiles of the dry flows are well represented by the Bagnold profile (Figure 10). For the wet flows, the fit quality of the Bagnold profile decreases as flow volume increases. This suggests that the wet flows of small source volume behaved similar to dry flows with collisional behavior throughout the flow height. As source volume increases, the velocity profiles depart from Bagnold and display a stronger $\dot{\gamma}$ at lower depth ($z/H \lesssim 0.4$) and a lower $\dot{\gamma}$ at higher depth. This would lead to a variation in I with flow height: higher I near the base and lower I near the free surface. This supports the finding that with the increase in source volume, a transition occurs from collisional behavior throughout the flow height, toward a complex flow regime where the lower portion remains collisional and the top portion is frictional.

While the flows were indeed granular, we next check the potential applicability of a fluid mechanics approach to model the fluidized behavior on a macroscopic scale. A Herschel-Bulkley profile, derived from the mechanics of a non-Newtonian fluid with a critical yield stress τ_c, was also tested for ability to replicate the flow shapes of the larger wet flows. The Herschel-Bulkey model has the general form (Coussot, 1994):

$$\tau = \tau_c + K(\dot{\gamma})^n \tag{5}$$

where K is the consistency coefficient, n is an exponent, and $\dot{\gamma}$ is the shear strain rate. The critical yield stress τ_c leads to a flow with an unsheared surface layer ("plug"). The profiles were plotted in the form of de Freitas Maciel et al. (2013) with a as a velocity scaling coefficient and h the total flow height. The thickness y_0 of the unsheared region is:

$$y_0 = h - \tau_c/a \tag{6}$$

For the sheared region with $0 \leq y \leq y_0$:

$$u(y) = \frac{n}{n+1} \left(\frac{a}{K} y_0^{(n+1)} \right)^{\frac{1}{n}} \left[1 - \left(1 - \frac{y}{y_0} \right)^{\frac{n+1}{n}} \right] \tag{7}$$

For the unsheared region with $y_0 \leq y \leq h$:

$$u(y) = \frac{n}{n+1} \left(\frac{a}{K} y_0^{(n+1)} \right)^{\frac{1}{n}} \tag{8}$$

When compared to the Bagnold profile in Figure 10, the Herschel-Bulkley profile is able to produce a profile more similar to the wet flows of the current study toward the top of the flow. Surface tension of the remaining water on and between the particles (i.e., the "residual water content" in unsaturated soil mechanics) may be acting as a critical yield stress above the top of fluid. The fit quality is less in the lower portion of the flow due to the lack of basal slip velocity in the formulation, a holdover from fluid mechanics.

7.3. Comparison of Results With Previous Experiments

The normalized velocity profiles in Figure 10 can be compared with previous experiments on saturated coarse-grained material. Velocity profiles were reported for steady-state experimental solid bed flows by Armanini et al. (2005). The normalized Armanini et al. profile is of a similar shape to the wet flows in the current study. Notable features include a non-zero basal slip velocity and a concave-up shape (shear strain rate decreases as height increases). Kaitna et al. (2014) tested five mixtures in a rotating drum (vertically rotating flume). The most similar mixture was of 4 mm gravel and water, which also displayed a concave-up shape but had a wider normalized velocity distribution than observed in the current study. In the rotating drum, the basal slip velocity is influenced by roughness intentionally added to aid recirculation in the drum.

Dimensionless numbers can help to assess the dominant source of flow resistance and serve as a mean of comparison to other experimental and natural flows. Two similar dimensionless numbers have been proposed that relate grain collisional stress to the confining pressure. Savage and Hutter (1989) first defined the Savage number N_{Sav} for a distinct shearing layer, where U is the velocity difference across the shearing layer, H_s is the shearing layer thickness, and d_p is the characteristic particle diameter:

$$N_{Sav} = \frac{\rho_s d_p^2 (U/H_s)^2}{P} \tag{9}$$

The Savage Number is equal to I^2 when the shear strain rate is taken as an average over a shear zone. Savage and Hutter (1989) proposed to classify shearing layers of dry granular flows by this parameter: collisional ($N_{Sav} > 0.1$) or frictional and ($N_{Sav} \leq 0.1$). Iverson and LaHusen (1993) extended the inference for debris flows, using depth-averaged parameters over the entire flow height rather than a distinct shearing layer of maximal shear strain rate by evaluating Equation 9 with H_s equal to the flow height, U the free surface velocity and P the total stress at the base $= \rho_s \nu H_s$ where ν is the average solid volume fraction over the flow height. This simplification is understandable, if not required, as the free-surface velocity and flow height are easier to measure for opaque and/or natural debris flows than a full velocity profile. We later refer to this as the depth-averaged basis.

The basal and free surface velocities and depth-averaged volume fractions are detailed for each trial in Table S1 of Supporting Information S1. Table S1 in Supporting Information S1 then presents N_{Sav} for each trial following Turnbull et al. (2015), where the confining pressure for wet flows is reduced following the concept of geotechnical effective stress:

$$N_{Sav} = \frac{\rho_s}{\rho_s - \rho_f} \frac{d_p^2 (\upsilon_{free} - \upsilon_{base})^2}{g h^3} \tag{10}$$

The observed depth-averaged N_{Sav} ranged from 0.46 to 0.22 for dry and 1.31 to 0.11 for wet. The larger flows tended to have lower N_{Sav}. For comparison, Iverson and Denlinger (2001) reported depth-averaged N_{Sav} of 0.2 for the United States Geological Survey (USGS) large outdoor flume experiments. On the depth-averaged basis, all flows in the current study were classified as collisional flows ($N_{Sav} > 0.1$). However, with the knowledge of the velocity profiles of the current study displaying a strong variation of $\dot{\gamma}$ with depth (Figure 10), it is clear that a shearing layer of high $\dot{\gamma}$ has formed. The use of the original Savage and Hutter (1989) definition would be more informative to classify the lightly and highly shearing zones than the depth-averaged basis.

The Bagnold Number, defined as in de Haas et al. (2015), Sanvitale and Bowman (2017), and Baselt et al. (2022), compares grain collision stresses with viscous fluid stresses:

$$N_{Bag} = \frac{\nu}{1 - \nu} \frac{\rho_s \dot{\gamma} d_p^2}{\mu} \tag{11}$$

where $\mu = 1$ mPa $\cdot$ s is the dynamic viscosity of water. The Bagnold numbers of the wet flows ranged between 6×10^2 and 1×10^3, once again classifying all the experiments as collisional by $N_{Bag} > 450$ (Iverson & Denlinger, 2001) as opposed to macroviscous ($N_{Bag} < 40$) or transitional ($40 < N_{Bag} < 450$). The USGS flume study was reported by Iverson and Denlinger as $N_{Bag} = 6 \times 10^2$, who also reported higher N_{Bag} for natural flows. Thus, the experiments of the current study are in line with the larger experimental flows and in the same "collisional" classification as the natural flows.

7.4. Implications to Natural Flows

Finally, we consider the potential implications to granular mass flows in the field and whether these findings would have implications on debris flows where a wider range of particle sizes are present and the interstitial fluid may be affected by fines.

The dimensionless numbers can be used to place the experimental flows in context with documented natural flows. Iverson and Denlinger (2001) reported N_{Sav} ranging between 0.001 and 0.06 for three well-documented natural wet granular flows. The variance over two orders of magnitude suggests that scaling effects are likely present between the largest experiments and field-scale. Some discrepancy may be due to the choice of a characteristic d_p for a polydisperse material (e.g., Sanvitale & Bowman, 2017). The much lower magnitudes of N_{Sav} for field-scale wet granular flows suggest that the thicker flows do suppress the collisional regime with sufficient confining pressure. However, for the reasons discussed above in Section 7.2, such a conclusion may be premature without a review of velocity profile measurements especially considering the normalized velocity profile results of the current study (Figure 10) do not show a constant shear strain rate but instead show a variation in shear strain rate with depth that is stronger than Bagnold scaling.

Unfortunately, velocity profile measurements of natural granular flows or debris flows are rare, especially for a non-erodible (solid) bed. Figure 10 includes the shape of the normalized velocity profiles for a natural debris flow over a non-erodible bed and an experiment with similar material to a natural debris flow. Nagl et al. (2020) used cross-correlation of paired conductivity sensors to measure an average velocity profile of a natural debris flow in an instrumented catchment. The reported d_{50} of the material was 0.15 m and the peak flow height was 0.9 m. The Nagl et al. data has a normalized velocity profile that is similar to Bagnold scaling, suggesting that the debris flow observed had large portions of granular materials that dominated flow behavior. The relatively small ratio of peak flow height to d_p may cause the flow to behave similar to the smaller wet flows in this study. Kaitna et al. (2014) tested a wide particle size distribution based on a natural debris flow in ("Wide GSD") in the rotating drum. The wet flows of the current study have similar normalized shapes as a large scale natural debris flow data, with nonzero basal slip velocity and a decreasing $\dot{\gamma}$ with increasing height above the base. The Kaitna et al. Wide GSD data shows a variation of $\dot{\gamma}$ over depth that exceeds the Bagnold profile and would therefore have a variation of I with depth similar to the larger wet flows in this study. From these comparisons, we see that collisional behavior may be present in field scale, natural debris flows and even the shape of the velocity profile may vary with flow thickness.

Engineering hazard assessment for debris flows often relies on depth-averaged runout models (e.g., Barnhart et al., 2021) to interpret recent events or to forecast runout or impact pressures. In these models, the shape of the velocity profile is represented via a shape coefficient. Further calibration is necessary to increase the accuracy of the depth-averaged momentum predicted by such models as more data becomes available for the velocity profiles of natural flows.

8. Conclusions

A series of monodisperse granular flows was released within a large laboratory flume to define the effect of landslide volume on the runout distance and the relative contributions of translation and spreading in the end member case of high permeability material. Both dry and initially saturated states were tested and the source volume was systematically varied from 0.2 to 1.0 m³ in 0.2 m³ increments. The use of high permeability granular material retained the possible influences of particle buoyancy and fluid drag but was confirmed to not result in basal fluid pressures that exceed hydrostatic conditions. The tests exhibited marked differences in runout distance and flow regimes as observed by high-speed video between dry and initially water saturated conditions. The initially saturated flows displayed an increase in flow velocity and runout distance as flow source volume increased. This

increase in total mobility was seen to come more from translation of the center-of-mass than spreading at the front.

The results show that the lower portions of the wet flows have decreased in volume fraction significantly and have entered a collisional regime. The shear strain rate $\dot{\gamma}$ is highest in the collisional zone near the base. The variation in flow speed and translation distance may be caused by partitioning of the source volume into generally (a) a highly shearing base, (b) a core section above, and (c) a slow tail section. A flow arrests itself when all the initial gravitational potential energy that was converted to kinetic energy is expended through friction, fluid drag, and other wasteful processes. Frictional energy expenditure is the product of the frictional force and the shear strain rate. By this, our velocity profile results show that energy expenditure is concentrated in the base of the flow. The slow tail section starves the flow of fluid and particles as the flume surface is wet and the particles remain by capillary forces. The remainder of the source volume is transported in the core very quickly with little energy expenditure due to the low shear strain rate, and is the prime contributor to the long runout distances observed. This system of flow regimes is considered to be a preferred, efficient state of flow. The decrease in effective flow resistance with increasing source volume is postulated to arise when varying source volumes are not split into these regimes proportionally: the experiments showed the highly shearing base to be of similar height across the series of wet flows and the tail sections appeared similar as well. Thus, a larger proportion of the source volume of larger flows is in the core section above the base and can move quickly with little energy expenditure.

Given that the data show strong variations in depth profiles of velocity and volume fraction, modeling approaches which consider particles and interstitial fluid on a macro-scale (such as a geotechnical continuum approach) or instead assume constant parameters over the depth of the flow (depth-averaged approach) might not adequately capture this behavior. Physical experiments linking particulate behavior to bulk response are required to fully validate and calibrate conceptual and numerical models of collisional and multiphase behavior. Experiments to evaluate the influence of basal roughness on the velocity profile, which is beyond the scope of this study, would provide additional data to better understand the role of basal friction and basal slip on the shape of the velocity profiles.

Flume experiments will remain useful for debris flow research for the foreseeable future. This data provides additional support to the conclusion that changes in flow thickness of fluid saturated flows, even within the range generally expected in laboratory experiments, can greatly change the effective flow resistance. This study begins to address the paucity of such experiments through the publication of a unique data set that combines the detailed grain-scale visual observations of flow structure, velocity, and volume fraction, with the observed consequences in terms of effective friction and material spreading. This unique data set (A. Taylor-Noonan, 2022) is publicly available on the Scholarsportal Dataverse repository to serve as a well-defined test scenario to assess the role of interstitial fluid in numerical runout models of debris flows.

Data Availability Statement

The data used in this research (A. Taylor-Noonan, 2022) are archived in the Queen's University Dataverse: https://doi.org/10.5683/SP3/1ZCUFY.

References

Allen, S. M., & Thomas, E. L. (1999). *The structure of materials* (Vol. 44). Wiley.

Alonso, E. E., Zervos, A., & Pinyol, N. M. (2016). Thermo-poro-mechanical analysis of landslides: From creeping behaviour to catastrophic failure. *Géotechnique*, *66*(3), 202–219. https://doi.org/10.1680/jgeot.15.lm.006

Ancey, C. (2007). Plasticity and geophysical flows: A review. *Journal of Non-Newtonian Fluid Mechanics*, *142*(1–3), 4–35. https://doi.org/10.1016/j.jnnfm.2006.05.005

Ancey, C., & Evesque, P. (2000). Frictional-collisional regime for granular suspension flows down an inclined channel. *Physical Review E*, *62*(6), 8349–8360. https://doi.org/10.1103/physreve.62.8349

Armanini, A. (2013). Granular flows driven by gravity. *Journal of Hydraulic Research*, *51*(2), 111–120. https://doi.org/10.1080/00221686.2013.788080

Armanini, A., Capart, H., Fraccarollo, L., & Larcher, M. (2005). Rheological stratification in experimental free-surface flows of granular–liquid mixtures. *Journal of Fluid Mechanics*, *532*, 269–319. https://doi.org/10.1017/s0022112005004283

Bagnold, R. (1954). Experiments on a gravity-free dispersion of large solid spheres in a Newtonian fluid under shear. *Proceedings of the Royal Society of London. Series A. Mathematical and Physical Sciences*, *225*(1160), 49–63. https://doi.org/10.1098/rspa.1954.0186

Barnhart, K. R., Jones, R. P., George, D. L., McArdell, B. W., Rengers, F. K., Staley, D. M., & Kean, J. W. (2021). Multi-model comparison of computed debris flow runout for the 9 January 2018 Montecito, California post-wildfire event. *Journal of Geophysical Research: Earth Surface*, *126*(12). https://doi.org/10.1029/2021jf006245

Bartelt, P., Buser, O., & Platzer, K. (2007). Starving avalanches: Frictional mechanisms at the tails of finite-sized mass movements. *Geophysical Research Letters*, *34*(20), L20407. https://doi.org/10.1029/2007gl031352

Baselt, I., de Oliveira, G. Q., Fischer, J.-T., & Pudasaini, S. P. (2022). Deposition morphology in large-scale laboratory stony debris flows. *Geomorphology*, *396*, 107992. https://doi.org/10.1016/j.geomorph.2021.107992

Bowman, E., Take, W., Rait, K., & Hann, C. (2012). Physical models of rock avalanche spreading behaviour with dynamic fragmentation. *Canadian Geotechnical Journal*, *49*(4), 460–476. https://doi.org/10.1139/t2012-007

Brevis, W., Niño, Y., & Jirka, G. H. (2010). Integrating cross-correlation and relaxation algorithms for particle tracking velocimetry. *Experiments in Fluids*, *50*(1), 135–147. https://doi.org/10.1007/s00348-010-0907-z

Bryant, S. K., Take, W. A., & Bowman, E. T. (2015). Observations of grain-scale interactions and simulation of dry granular flows in a large-scale flume. *Canadian Geotechnical Journal*, *52*(5), 638–655. https://doi.org/10.1139/cgj-2013-0425

Caballero, L., Sarocchi, D., Soto, E., & Borselli, L. (2014). Rheological changes induced by clast fragmentation in debris flows. *Journal of Geophysical Research: Earth Surface*, *119*(9), 1800–1817. https://doi.org/10.1002/2013jf002942

Capart, H., Young, D. L., & Zech, Y. (2002). Voronoï imaging methods for the measurement of granular flows. *Experiments in Fluids*, *32*(1), 121–135. https://doi.org/10.1007/s003480200013

Chialvo, S., Sun, J., & Sundaresan, S. (2012). Bridging the rheology of granular flows in three regimes. *Physical Review E*, *85*(2), 021305. https://doi.org/10.1103/physreve.85.021305

Coombs, S. (2018). *A physical investigation of the flow structure and mobility behaviour of collisional granular landslides* (MA thesis). Queen's University.

Coombs, S., Apostolov, A., Take, W. A., & Benoît, J. (2019). Mobility of dry granular flows of varying collisional activity quantified by smart rock sensors. *Canadian Geotechnical Journal*, *57*(10), 1484–1496. https://doi.org/10.1139/cgj-2018-0278

Corominas, J. (1996). The angle of reach as a mobility index for small and large landslides. *Canadian Geotechnical Journal*, *33*(2), 260–271. https://doi.org/10.1139/t96-005

Coussot, P. (1994). Steady, laminar, flow of concentrated mud suspensions in open channel. *Journal of Hydraulic Research*, *32*(4), 535–559. https://doi.org/10.1080/00221686.1994.9728354

Dade, W. B., & Huppert, H. E. (1998). Long-runout rockfalls. *Geology*, *26*(9), 803. https://doi.org/10.1130/0091-7613(1998)026<0803:lrr>2.3.co;2

de Freitas Maciel, G., de Oliveira Ferreira, F., & Fiorot, G. H. (2013). Control of instabilities in non-Newtonian free surface fluid flows. *Journal of the Brazilian Society of Mechanical Sciences and Engineering*, *35*(3), 217–229. https://doi.org/10.1007/s40430-013-0025-y

de Haas, T., Braat, L., Leuven, J. R. F. W., Lokhorst, I. R., & Kleinhans, M. G. (2015). Effects of debris flow composition on runout, depositional mechanisms, and deposit morphology in laboratory experiments. *Journal of Geophysical Research: Earth Surface*, *120*(9), 1949–1972. https://doi.org/10.1002/2015jf003525

Fischer, J.-T., Kaitna, R., Heil, K., & Reiweger, I. (2018). The heat of the flow: Thermal equilibrium in gravitational mass flows. *Geophysical Research Letters*, *45*(20), 11219–11226. https://doi.org/10.1029/2018gl079585

Forterre, Y., & Pouliquen, O. (2008). Flows of dense granular media. *Annual Review of Fluid Mechanics*, *40*(1), 1–24. https://doi.org/10.1146/annurev.fluid.40.111406.102142

GDR MiDi. (2004). On dense granular flows. *The European Physical Journal E*, *14*(4), 341–365. https://doi.org/10.1140/epje/i2003-10153-0

Gollin, D., Brevis, W., Bowman, E. T., & Shepley, P. (2017). Performance of PIV and PTV for granular flow measurements. *Granular Matter*, *19*(3), 42. https://doi.org/10.1007/s10035-017-0730-9

Goren, L., & Aharonov, E. (2007). Long runout landslides: The role of frictional heating and hydraulic diffusivity. *Geophysical Research Letters*, *34*(7), L07301. https://doi.org/10.1029/2006gl028895

Hotta, N. (2012). Basal interstitial water pressure in laboratory debris flows over a rigid bed in an open channel. *Natural Hazards and Earth System Sciences*, *12*(8), 2499–2505. https://doi.org/10.5194/nhess-12-2499-2012

Hungr, O. (1995). A model for the runout analysis of rapid flow slides, debris flows, and avalanches. *Canadian Geotechnical Journal*, *32*(4), 610–623. https://doi.org/10.1139/t95-063

Hungr, O., Leroueil, S., & Picarelli, L. (2013). The Varnes classification of landslide types, an update. *Landslides*, *11*(2), 167–194. https://doi.org/10.1007/s10346-013-0436-y

Hürlimann, M., McArdell, B. W., & Rickli, C. (2015). Field and laboratory analysis of the runout characteristics of hillslope debris flows in Switzerland. *Geomorphology*, *232*, 20–32. https://doi.org/10.1016/j.geomorph.2014.11.030

Iverson, R. M. (1997). The physics of debris flows. *Reviews of Geophysics*, *35*(3), 245–296. https://doi.org/10.1029/97rg00426

Iverson, R. M. (2015). Scaling and design of landslide and debris-flow experiments. *Geomorphology*, *244*, 9–20. https://doi.org/10.1016/j.geomorph.2015.02.033

Iverson, R. M., & Denlinger, R. P. (2001). Flow of variably fluidized granular masses across three-dimensional terrain: 1. Coulomb mixture theory. *Journal of Geophysical Research*, *106*(B1), 537–552. https://doi.org/10.1029/2000jb900329

Iverson, R. M., & LaHusen, R. G. (1993). Friction in debris flows: Inferences from large-scale flume experiments. In H. W. Shen, S. T. Su, & F. Wen (Eds.), *Proceedings - National Conference on Hydraulic Engineering* (pp. 1604–1609). American Society of Civil Engineers.

Iverson, R. M., Logan, M., LaHusen, R. G., & Berti, M. (2010). The perfect debris flow? Aggregated results from 28 large-scale experiments. *Journal of Geophysical Research*, *115*(F3), F03005. https://doi.org/10.1029/2009jf001514

Jenkins, J. T. (2007). Dense inclined flows of inelastic spheres. *Granular Matter*, *10*(1), 47–52. https://doi.org/10.1007/s10035-007-0057-z

Jenkins, J. T., & Savage, S. B. (1983). A theory for the rapid flow of identical, smooth, nearly elastic, spherical particles. *Journal of Fluid Mechanics*, *130*, 187. https://doi.org/10.1017/s0022112083001044

Kaitna, R., Dietrich, W. E., & Hsu, L. (2014). Surface slopes, velocity profiles and fluid pressure in coarse-grained debris flows saturated with water and mud. *Journal of Fluid Mechanics*, *741*, 377–403. https://doi.org/10.1017/jfm.2013.675

Kaitna, R., Palucis, M. C., Yohannes, B., Hill, K. M., & Dietrich, W. E. (2016). Effects of coarse grain size distribution and fine particle content on pore fluid pressure and shear behavior in experimental debris flows. *Journal of Geophysical Research: Earth Surface*, *121*(2), 415–441. https://doi.org/10.1002/2015jf003725

Kesseler, M., Heller, V., & Turnbull, B. (2020). Grain Reynolds Number scale effects in dry granular slides. *Journal of Geophysical Research: Earth Surface*, *125*(1), e2019JF005347. https://doi.org/10.1029/2019jf005347

Lanzoni, S., Gregoretti, C., & Stancanelli, L. M. (2017). Coarse-grained debris flow dynamics on erodible beds. *Journal of Geophysical Research: Earth Surface*, *122*(3), 592–614. https://doi.org/10.1002/2016jf004046

Legros, F. (2002). The mobility of long-runout landslides. *Engineering Geology*, *63*(3–4), 301–331. https://doi.org/10.1016/s0013-7952(01)00090-4

Leonardi, A., Cabrera, M., Wittel, F. K., Kaitna, R., Mendoza, M., Wu, W., & Herrmann, H. J. (2015). Granular-front formation in free-surface flow of concentrated suspensions. *Physical Review E*, *92*(5), 052204. https://doi.org/10.1103/physreve.92.052204

Lun, C. K. K. (1991). Kinetic theory for granular flow of dense, slightly inelastic, slightly rough spheres. *Journal of Fluid Mechanics*, *233*, 539–559. https://doi.org/10.1017/s0022112091000599

Lun, C. K. K., & Savage, S. B. (1986). The effects of an impact velocity dependent coefficient of restitution on stresses developed by sheared granular materials. *Acta Mechanica*, *63*(1–4), 15–44. https://doi.org/10.1007/bf01182538

Lyu, L., Wang, Z., Cui, P., & Xu, M. (2017). The role of bank erosion on the initiation and motion of gully debris flows. *Geomorphology*, *285*, 137–151. https://doi.org/10.1016/j.geomorph.2017.02.008

Mangeney, A., Roche, O., Hungr, O., Mangold, N., Faccanoni, G., & Lucas, A. (2010). Erosion and mobility in granular collapse over sloping beds. *Journal of Geophysical Research*, *115*(F3), F03040. https://doi.org/10.1029/2009jf001462

McArdell, B. W., Bartelt, P., & Kowalski, J. (2007). Field observations of basal forces and fluid pore pressure in a debris flow. *Geophysical Research Letters*, *34*(7), L07406. https://doi.org/10.1029/2006gl029183

McDougall, S. (2017). 2014 Canadian Geotechnical Colloquium: Landslide runout analysis—Current practice and challenges. *Canadian Geotechnical Journal*, *54*(5), 605–620. https://doi.org/10.1139/cgj-2016-0104

Nagl, G., Hübl, J., & Kaitna, R. (2020). Velocity profiles and basal stresses in natural debris flows. *Earth Surface Processes and Landforms*, *45*(8), 1764–1776. https://doi.org/10.1002/esp.4844

Parez, S., & Aharonov, E. (2015). Long runout landslides: A solution from granular mechanics. *Frontiers in Physics*, *3*, 80. https://doi.org/10.3389/fphy.2015.00080

Pastor, M., Blanc, T., Haddad, B., Drempetic, V., Morles, M. S., Dutto, P., et al. (2014). Depth averaged models for fast landslide propagation: Mathematical, rheological and numerical aspects. *Archives of Computational Methods in Engineering*, *22*(1), 67–104. https://doi.org/10.1007/s11831-014-9110-3

Pudasaini, S. P., Wang, Y., & Hutter, K. (2005). Modelling debris flows down general channels. *Natural Hazards and Earth System Sciences*, *5*(6), 799–819. https://doi.org/10.5194/nhess-5-799-2005

Raymond, G. P. (2002). Reinforced ballast behaviour subjected to repeated load. *Geotextiles and Geomembranes*, *20*(1), 39–61. https://doi.org/10.1016/s0266-1144(01)00024-3

Rickenmann, D. (2011). Runout prediction methods. In O. Hungr & M. Jakob (Eds.), *Debris-flow hazards and related phenomena* (pp. 305–324). Springer Berlin Heidelberg.

Rowe, R. K., Ashe, L., Take, W. A., & Brachman, R. (2014). Factors affecting the down-slope erosion of bentonite in a GCL. *Geotextiles and Geomembranes*, *42*(5), 445–456. https://doi.org/10.1016/j.geotexmem.2014.07.002

Sanvitale, N., & Bowman, E. T. (2017). Visualization of dominant stress-transfer mechanisms in experimental debris flows of different particle-size distribution. *Canadian Geotechnical Journal*, *54*(2), 258–269. https://doi.org/10.1139/cgj-2015-0532

Savage, S. B., & Hutter, K. (1989). The motion of a finite mass of granular material down a rough incline. *Journal of Fluid Mechanics*, *199*, 177–215. https://doi.org/10.1017/s0022112089000340

Shugar, D. H., Jacquemart, M., Shean, D., Bhushan, S., Upadhyay, K., Sattar, A., et al. (2021). A massive rock and ice avalanche caused the 2021 disaster at Chamoli, Indian Himalaya. *Science*, *373*(6552), 300–306. https://doi.org/10.1126/science.abh4455

Staron, L., & Lajeunesse, E. (2009). Understanding how volume affects the mobility of dry debris flows. *Geophysical Research Letters*, *36*(12), L12402. https://doi.org/10.1029/2009gl038229

Taylor-Noonan, A. (2022). Experimental data of dry and saturated granular flows of increasing source volume [Dataset] Scholars Portal Dataverse. https://doi.org/10.5683/SP3/1ZCUFY

Taylor-Noonan, A. M., Gollin, D., Bowman, E. T., & Take, W. A. (2021). The influence of image analysis methodology on the calculation of granular temperature for granular flows. *Granular Matter*, *23*(4), 96. https://doi.org/10.1007/s10035-021-01153-y

Tayyebi, S. M., Pastor, M., & Stickle, M. M. (2021). Two-phase SPH numerical study of pore-water pressure effect on debris flows mobility: Yu Tung debris flow. *Computers and Geotechnics*, *132*, 103973. https://doi.org/10.1016/j.compgeo.2020.103973

Tsubaki, T., Hashimoto, H., & Suetsugi, T. (1983). Interparticle stresses and characteristics of debris flow. *Journal of Hydroscience and Hydraulic Engineering*, *1*(2), 67–82.

Turnbull, B., Bowman, E. T., & McElwaine, J. N. (2015). Debris flows: Experiments and modelling. *Comptes Rendus Physique*, *16*(1), 86–96. https://doi.org/10.1016/j.crhy.2014.11.006

Voight, B., & Faust, C. (1982). Frictional heat and strength loss in some rapid landslides. *Géotechnique*, *32*(1), 43–54. https://doi.org/10.1680/geot.1982.32.1.43

Walter, F., Amann, F., Kos, A., Kenner, R., Phillips, M., de Preux, A., et al. (2020). Direct observations of a three million cubic meter rock-slope collapse with almost immediate initiation of ensuing debris flows. *Geomorphology*, *351*, 106933. https://doi.org/10.1016/j.geomorph.2019.106933

Zheng, H., Shi, Z., Hanley, K. J., Peng, M., Guan, S., Feng, S., & Chen, K. (2021). Deposition characteristics of debris flows in a lateral flume considering upstream entrainment. *Geomorphology*, *394*, 107960. https://doi.org/10.1016/j.geomorph.2021.107960

Zhou, G. G. D., Li, S., Song, D., Choi, C. E., & Chen, X. (2018). Depositional mechanisms and morphology of debris flow: Physical modelling. *Landslides*, *16*(2), 315–332. https://doi.org/10.1007/s10346-018-1095-9